Attribution of Atmospheric Variations in the 1997–2003 Period to SST Anomalies in the Pacific and Indian Ocean Basins

NGAR-CHEUNG LAU, ANTS LEETMAA, AND MARY JO NATH

NOAA/Geophysical Fluid Dynamics Laboratory, Princeton University, Princeton, New Jersey

(Manuscript received 17 May 2005, in final form 1 November 2005)

ABSTRACT

The individual impacts of sea surface temperature (SST) anomalies in the deep tropical eastern–central Pacific (DTEP) and Indo-western–central Pacific (IWP) on the evolution of the observed global atmospheric circulation during the 1997–2003 period have been investigated using a new general circulation model. Ensemble integrations were conducted with monthly varying SST conditions being prescribed separately in the DTEP sector, the IWP sector, and throughout the World Ocean. During the 1998–2002 subperiod, when prolonged La Niña conditions occurred in DTEP and the SST in IWP was above normal, the simulated midlatitude atmospheric responses to SST forcing in the DTEP and IWP sectors reinforced each other. The anomalous geopotential height ridges at 200 mb in the extratropics of both hemispheres exhibited a distinct zonal symmetry. This circulation change was accompanied by extensive dry and warm anomalies in many regions, including North America. During the 1997–98 and 2002–03 El Niño events, the SST conditions in both DTEP and IWP were above normal, and considerable cancellations were simulated between the midlatitude responses to the oceanic forcing from these two sectors. The above findings are contrasted with those for the 1953–58 and 1972–77 periods, which were characterized by analogous SST developments in DTEP, but by cold conditions in IWP. It is concluded that a warm anomaly in IWP and a cold anomaly in DTEP constitute the optimal SST configuration for generating zonally elongated ridges in the midlatitudes.

Local diagnoses indicate that the imposed SST anomaly alters the strength of the zonal flow in certain longitudinal sectors, which influences the behavior of synoptic-scale transient eddies farther downstream. The modified eddy momentum transports in the regions of eddy activity in turn feed back on the local mean flow, thus contributing to its zonal elongation. These results are consistent with the inferences drawn from zonal mean analyses, which accentuate the role of the eddy-induced circulation on the meridional plane.

1. Introduction

Numerous observational and modeling studies have demonstrated that sea surface temperature (SST) anomalies in certain parts of the World Ocean exert considerable influences on atmospheric variations on time scales longer than a month. Much attention has been devoted to the effects of oceanic changes at two particular regions: the deep tropical eastern–central Pacific (DTEP), and the Indo-western–central Pacific (IWP). The DTEP region exhibits large SST variability on interannual time scales, primarily due to the occurrence of warm and cold El Niño–Southern Oscillation (ENSO) events in that location. The SST changes in the IWP sector may be linked to multiple causes, including local air–sea coupled modes (e.g., Saji et al. 1999; Webster et al. 1999), transmission of remote ENSO forcing to this region by atmospheric "bridges" spanning across the Pacific and Indian Oceans (e.g., Klein et al. 1999; Lau and Nath 2003; Alexander et al. 2002, 2004), and a prominent secular warming trend in recent decades (e.g., Knutson et al. 1999; Hoerling et al. 2004). Evidence presented by other investigators (e.g., Sutton and Hodson 2003, 2005; Rodwell et al. 1999) indicates that, in addition to the DTEP and IWP regions, the SST conditions in the Atlantic basin are also an important contributor to atmospheric variability.

The global atmospheric patterns associated with ENSO-related SST anomalies in DTEP have been exhaustively documented. Particularly noteworthy are the zonally symmetric upper-tropospheric responses within the tropical belt (Horel and Wallace 1981; Kumar and Hoerling 2003), as well as extratropical signals that are

Corresponding author address: Dr. Ngar-Cheung Lau, NOAA/Geophysical Fluid Dynamics Laboratory, Princeton University, Forrestal Campus, P.O. Box 308, Princeton, NJ 08542.
E-mail: gabriel.lau@noaa.gov

composed of both a zonal-mean component (e.g., Seager et al. 2003) and wavelike features (e.g., Horel and Wallace 1981; Trenberth et al. 1998; Nigam 2003). Considerable empirical evidence also exists on the sensitivity of the atmospheric circulation to SST variations in IWP. For instance, the SST anomalies in that region have been linked to fluctuations in the Asian monsoon (e.g., Weare 1979; Lau and Nath 2000; Kawamura et al. 2001a,b), delayed Tropics-wide tropospheric temperature responses after ENSO episodes (Kumar and Hoerling 2003), as well as changes in the North Atlantic climate (Hoerling et al. 2001; Lu et al. 2004).

Independent model experiments have recently been performed and analyzed by Hoerling and Kumar (2003), Seager et al. (2003), Schubert et al. (2004), and Lau et al. (2005, hereafter referred as L05), with the common goal of delineating the effects of tropical SST forcing on the global atmospheric circulation. A ubiquitous inference from these model studies is that the SST anomalies at various tropical sites (such as the DTEP or IWP), either by acting individually or in conjunction with each other, are capable of generating atmospheric anomalies with a notable degree of zonal symmetry at various latitude bands. Of special interest are the zonally extended upper-tropospheric ridges and troughs in the subtropics and extratropics of both hemispheres. These features are often coincident with widespread changes in precipitation and near-surface temperature. These and other model results indicate that DTEP and IWP are the "perfect oceans" for causing drought (Hoerling and Kumar 2003), and that tropical SST variability is an important factor for dry conditions in North America, of which the Dust Bowl in the 1930s (Schubert et al. 2004) and the severe 1988 drought (Trenberth and Branstator 1992) are prime examples. It should be stressed at the outset that, in addition to ENSO processes, other modes of oceanic variability could also yield zonally symmetric atmospheric responses. The relative roles of these distinct mechanisms in the formation of longitudinally extended anomalies remain to be fully assessed.

The evolution of the prominent SST anomalies over the Pacific and Indian Oceans during the 1997–2003 period offers an excellent opportunity for assessing their effects on the global atmosphere. The observed anomalous SST field in this period is illustrated in the left and right panels of Fig. 1a, which correspond to the IWP and DTEP sectors, respectively. At each longitude along the abscissa, the SST anomalies have been averaged over all maritime grid points between 5°S and 5°N in the right panel, and between 30°S and 30°N in the left panel. The anomalies represent departures from the 1971–2000 climatology. The right panel (165°E–70°W) shows that the period began with one of the strongest El Niño events of the twentieth century in 1997–98, and ended with a more modest warm event in 2002–03. In between these two episodes is a prolonged cold interval lasting for about four (three) years in the eastern (central) equatorial Pacific. The pattern in the 30°–165°E sector (left panel), which is based on averages over a broader range of latitudes, indicates that above-normal SST prevailed in IWP through almost the entire period.

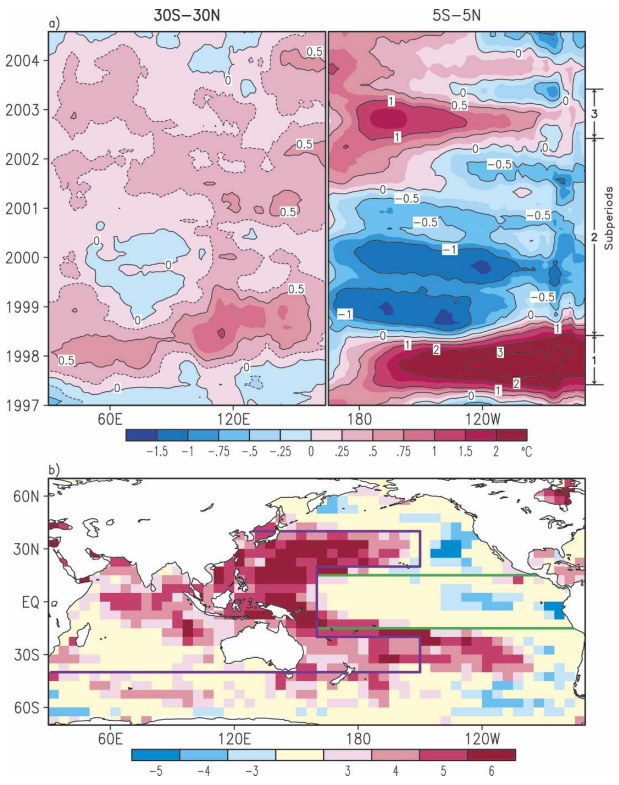

FIG. 1. (a) Time–longitude distributions of SST anomalies (right) in the central–eastern tropical Pacific sector, as obtained by averaging over the data between 5°S and 5°N, and (left) in the Indo-western Pacific sector, as obtained by averaging between 30°S and 30°N, for the 1997–2004 period. A 7-month running-mean smoothing has been applied. Solid contours indicate values of 0°, ±0.5°, ±1°, ±2°, and ±3°C. Dashed contours in the left panel indicate values of ±0.25°C. The span of subperiods 1, 2, and 3 is indicated along the right margin of the right panel. (b) Number of 12-month periods in June 1997–May 2003 with SST anomalies at individual 5° (lat) × 5° (lon) rectangles being above normal (red shading) or below normal (blue shading) by more than one-half of a std dev (0.5σ). Sites with anomalies surpassing 0.5σ in two 12-month periods or less; as well as sites with three warm and three cold 12-month periods exceeding 0.5σ, are indicated by yellow shading. The green and purple borders depict the domains in which interannual SST anomalies have been prescribed in the DTEP and IWP experiments, respectively.

To identify the locations of the SST sites that contribute most to the persistent signals seen in Fig. 1a, the SST anomalies at individual rectangles with latitudinal and longitudinal dimensions of 5° were computed for the 12-month interval from June of a given year to May of the following year. Such time averages were obtained for each of the six 12-month periods between June 1997 and May 2003. The standard deviation σ of the 12-month averages of the SST time series for 1971–2000 was also evaluated at individual sites. For each rectangle, the numbers of 12-month periods in 1997–2003 with positive and negative anomalies exceeding 0.5σ were then determined. Those locations with warm (cold) anomalies larger than 0.5σ in 3 or more 12-month periods are highlighted in Fig. 1b using red (blue) shading of varying intensity. This chart indicates that many of the sites in the tropical Pacific sector west of 165°E are characterized by warm anomalies during a large portion of the 1997–2003 period. Also evident from Fig. 1b (but not from the right panel of Fig. 1a), is the eastward extension of the prolonged warm anomalies within the 20°–40°S and 20°–40°N zonal belts in the central Pacific. In the DTEP zone, the SST remained below normal for three to four 12-month periods at some of the near-equatorial sites, reflecting the occurrence of successive La Niña episodes during 1998–2002.

In addition to the salient SST signatures depicted in Fig. 1, significant changes in the atmospheric climate have also been detected within the same period. Specifically, positive 200-mb height anomalies were observed at most longitudes in the midlatitude belts of both hemispheres throughout the 4-yr segment from June 1998 to May 2002 (Hoerling and Kumar 2003; see also Fig. 2a of the present paper). These zonally extended anomalous ridges were accompanied by widespread droughts and above-normal surface temperatures in the United States, the Mediterranean region and southwest Asia (Barlow et al. 2002; Hoerling and Kumar 2003; Figs. 4a,e of the present paper). In view of the above concomitant variations in SST, zonally symmetric circulation, as well as precipitation and surface air temperature over extensive areas, the phenomena in this period constitute an ideal testing ground of our current understanding of the air–sea relationships based on the recent observational and modeling studies.

The primary goal of the present study is to examine the mechanisms contributing to the rich array of oceanic and atmospheric signals in 1997–2003 as described above, and in analogous episodes occurring in earlier decades. We have made an effort to broaden the scope of other recent studies on this subject in the following aspects:

- In addition to the impacts of ENSO-related SST changes on atmospheric variability, which is the primary concern of the investigations by Seager et al. (2003) and Schubert et al. (2004), the substantial role of the oceanic forcing from the IWP sector is highlighted in our work.
- The pioneering study Hoerling and Kumar (2003) is focused on the 1998–2002 period, when the SST anomalies in DTEP and IWP were of opposite polarities. After substantiating their findings based on our new model results (section 3a), we proceed to examine the observed and simulated atmospheric responses in other SST forcing scenarios, such as the 1997–98 and 2002–03 El Niño events (when both DTEP and IWP sectors were warmer than normal, see section 3b), as well as the 1973–75 and 1954–56 La Niña episodes (when temperatures in both sectors were below normal, see section 4). This expanded set of case studies allow for a more complete survey of atmospheric responses to different combinations of SST forcings in DTEP and IWP.
- The SST anomalies in IWP as considered by L05 are generated by an oceanic mixed layer model, and are solely attributable to the ENSO forcing in DTEP through the "atmospheric bridge" mechanism. The SST changes in IWP as prescribed in the experiments for the present study are based on actual observations, and could be related to a variety of phenomena, among which the sustained oceanic warming in recent decades is of particular interest. Hence the current study addresses a broader set of issues on climate variability than that examined in L05. Differences between the temporal evolution of the imposed IWP forcings in L05 and in the present work also have implications on the seasonal dependence of the atmospheric responses (see Fig. 3), and on the climate anomalies occurring in the North Pacific–North American region (see section 5).
- The diagnoses on the contributions of eddy–mean flow interactions to zonally elongated atmospheric anomalies, as previously performed by Seager et al. (2003) and L05, are extended in the present investigation by comparing in greater depth the results based on forcings from the DTEP and IWP sectors separately (see section 6).
- The presentation of results in previous studies is mostly confined to ensemble-mean model responses. We hereby offer a detailed documentation of the range of responses simulated in individual members of a given ensemble experiment (see Figs. 5 and 8), so

as to assess the robustness of various atmospheric signals of interest.

2. Experimental design

The basic tool for this study is the new general circulation model constructed by the Geophysical Fluid Dynamics Laboratory (GFDL) Global Atmospheric Model Development Team (GAMDT). The dynamical and physical components of this atmosphere–land model version 2 (AM2–LM2), as well as its performance in replicating various essential aspects of the atmospheric climate, have been documented in detail by the GFDL Global Atmospheric Model Development Team (2004). This model uses a finite-difference formulation, with a resolution of 2° and 2.5° in the meridional and zonal directions, respectively. The processes incorporated in the AM2–LM2 include diurnal changes in radiative transfer, variations of different cloud species, convection as parameterized by a relaxed Arakawa–Schubert scheme, vertical exchanges within the atmospheric boundary layer, and soil–vegetation interactions.

The performance of the AM2–LM2 in simulating the midlatitude response in both hemispheres to ENSO forcing in the 1951–2000 period has been assessed by GFDL Global Atmospheric Model Development Team (2004, their Fig. 14) using regression charts of the 200-mb height field versus a SST index of ENSO. The principal anomaly centers in the observed pattern are reproduced in the model atmosphere, with good agreement with respect to geographical location and amplitude. The simulated center over the North Pacific has a more distinct east–west orientation as compared to the corresponding observation, thus resulting in a slightly stronger degree of zonal symmetry in the model result for the Northern Hemisphere. The ENSO-related atmospheric pattern based on AM2–LM2 may also be compared with that produced in experiments with a GFDL climate model of the previous generation, as documented by Lau and Nath (1994, their Figs. 5 and 8). The features in the North Pacific–North American sector are generally more realistic in the AM2–LM2 result.

The following three experiments have been conducted using the AM2–LM2.

a. GLOBAL experiment

The monthly varying SST conditions observed during the 1951–2004 period were sequentially inserted at grid points throughout the World Ocean. The SST input is based on the analyses compiled by Hurrell et al. (2005, manuscript submitted to *J. Climate*). Ten parallel integrations have been conducted with each of two recent versions (with the designations "11" and "12b") of the AM2–LM2. These individual runs were initiated from distinct sets of atmospheric conditions. Most of the numerical and physical schemes in versions 11 and 12b are similar to each other. The number of vertical levels has been increased from 18 (version 11) to 24 (version 12b). A modified planetary boundary scheme has been used in version 12b. In view of the strong consistency between the results based on the simulations of versions 11 and 12b separately (not shown), the output from the two versions have been combined, thus yielding an ensemble consisting of 20 individual members.

b. DTEP experiment

Thirty integrations have been performed for this experiment by using version 12b of AM2–LM2. The temporally varying SST forcing observed from 1997 to 2004 was prescribed only in the deep tropical eastern-central Pacific region in 15°S–15°N, and from 160°E to the American coast (see domain with green boundary in Fig. 1b). The interannual SST changes in this domain are primarily associated with evolution of ENSO episodes. The SST condition at all grid points lying outside of this region was constrained to evolve through climatological seasonal cycles in all years, as obtained from averages of the SST analyses produced by Hurrell et al. (2005, manuscript submitted to *J. Climate*) over the 1971–2000 period.

c. IWP experiment

Another 30 integrations have been conducted for this experiment. It is analogous to the DTEP experiment, except that the domain of variable SST forcing was relocated to the Indian Ocean and subtropical western–central Pacific sector. This region (see the purple boundary in Fig. 1b) encompasses the Indian and western Pacific Oceans between 40°S and 40°N, as well as extensions along the 20°–40° latitude zones in the North and South Pacific from 160°E to 150°W.

The results to be presented in the following sections (except for Figs. 5 and 8) are based on ensemble averages over the individual samples available for a given experiment. Anomalies have been computed by removing the appropriate climatology for the 1971–2000 period. Statistical significance of the anomalies examined in this study has been assessed by contrasting the ensemble-mean signal strength against the intersample variability within the ensemble of experiments (Student's *t* test). Most of the principal features noted in the following discussions exceed the 95%–99% confidence levels.

Some of the model findings in this study have been compared with the corresponding observational estimates. The latter datasets include the reanalyses of the 200-mb height and near-surface air temperature fields, as produced by the National Centers for Environmental Prediction–National Center for Atmospheric Research (NCEP–NCAR; see Kalnay et al. 1996), and the precipitation records analyzed by Dai et al. (1997) and the Global Precipitation Climatology Project (GPCP; see Huffman et al. 1997). For the NCEP–NCAR reanalyses, the anomalies were also obtained by removing the 1971–2000 climatology. Due to the shorter lengths of the Dai and GPCP datasets, the observed precipitation anomalies were computed using the climatologies for the 1950–95 and 1979–2000 periods, respectively.

3. Observed and simulated atmospheric anomalies in 1997–2003

In view of the marked differences seen in Fig. 1a between the SST anomaly pattern in 1998–2002 (with cold DTEP and warm IWP) and that in 1997–98 or 2002–03 (when both DTEP and IWP were warm), the atmospheric patterns in these individual subperiods are considered separately. We shall henceforth refer to the time intervals of June 1997–May 1998 as subperiod 1, June 1998–May 2002 as subperiod 2, and June 2002–May 2003 as subperiod 3. The temporal span of these subperiods is indicated in the right margin of Fig. 1a.

a. 1998–2002 subperiod

The distributions of the anomalous 200-mb height for subperiod 2, as obtained from (Fig. 2a) NCEP–NCAR observational reanalyses, and from simulations in the (Fig. 2b) GLOBAL, (Fig. 2c) DTEP, and (Fig. 2d) IWP experiments, are displayed in Fig. 2. The most prominent features in the observed pattern (Fig. 2a) are the pair of positive height anomalies circumscribing almost the entire latitude zones in 20°–40°N and 30°–50°S. Negative height anomalies prevail in the vicinity of the DTEP region. The zonally extended anomalous ridges are well simulated in the GLOBAL experiment (Fig. 2b), whereas the negative center over the central tropical Pacific in the model atmosphere is weaker than its observed counterpart. The elongated ridges in the subtropical–midlatitude belt of the two hemispheres are evident in Figs. 2c,d. However, the amplitude of the extratropical response to SST changes in IWP is noticeably higher than that to forcing in the DTEP sector. The prolonged La Niña conditions prescribed in the DTEP experiment are seen to yield negative height anomalies throughout the Tropics along the equator

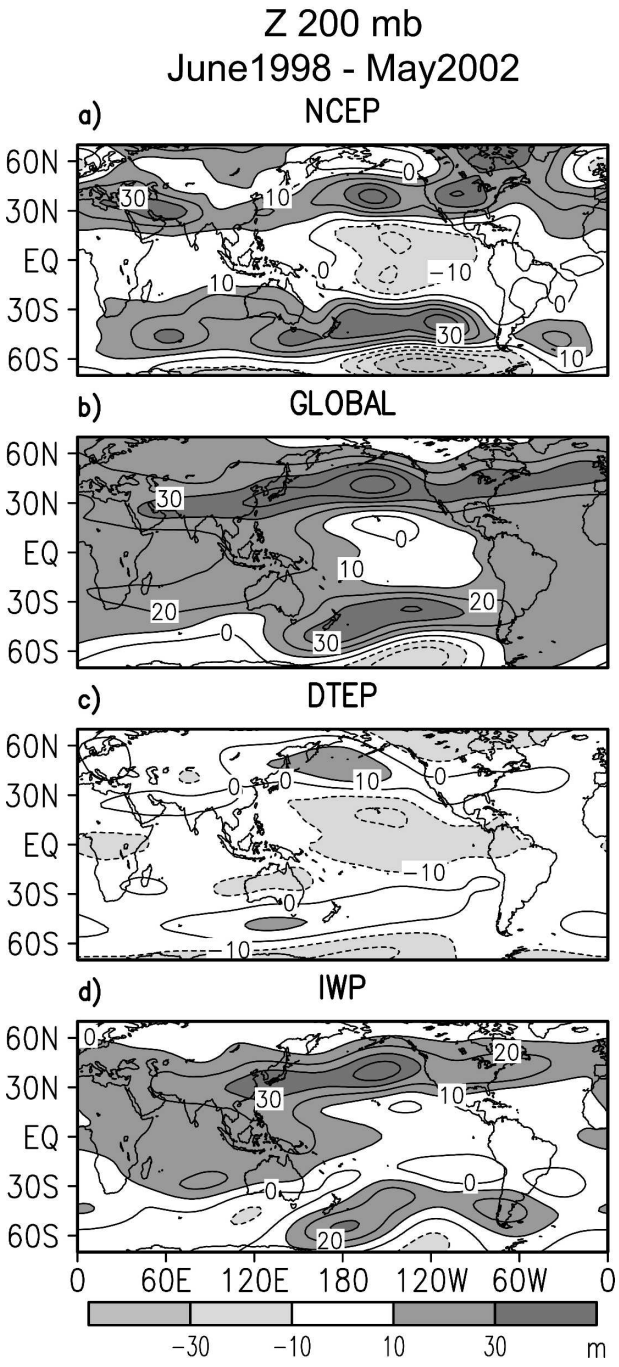

FIG. 2. Horizontal distributions of 200-mb height anomaly in June 1998–May 2003 (subperiod 2), as obtained from (a) NCEP–NCAR reanalyses, and model simulations in the (b) GLOBAL, (c) DTEP, and (d) IWP experiments. Contour interval: 10 m.

(Fig. 2c); whereas the persistent warmth in the IWP sector generates mostly positive anomalies (Fig. 2d). The spatial correlation coefficients between the GLOBAL (Fig. 2b) and IWP (Fig. 2d) patterns, and between the GLOBAL and DTEP (Fig. 2c) patterns, are

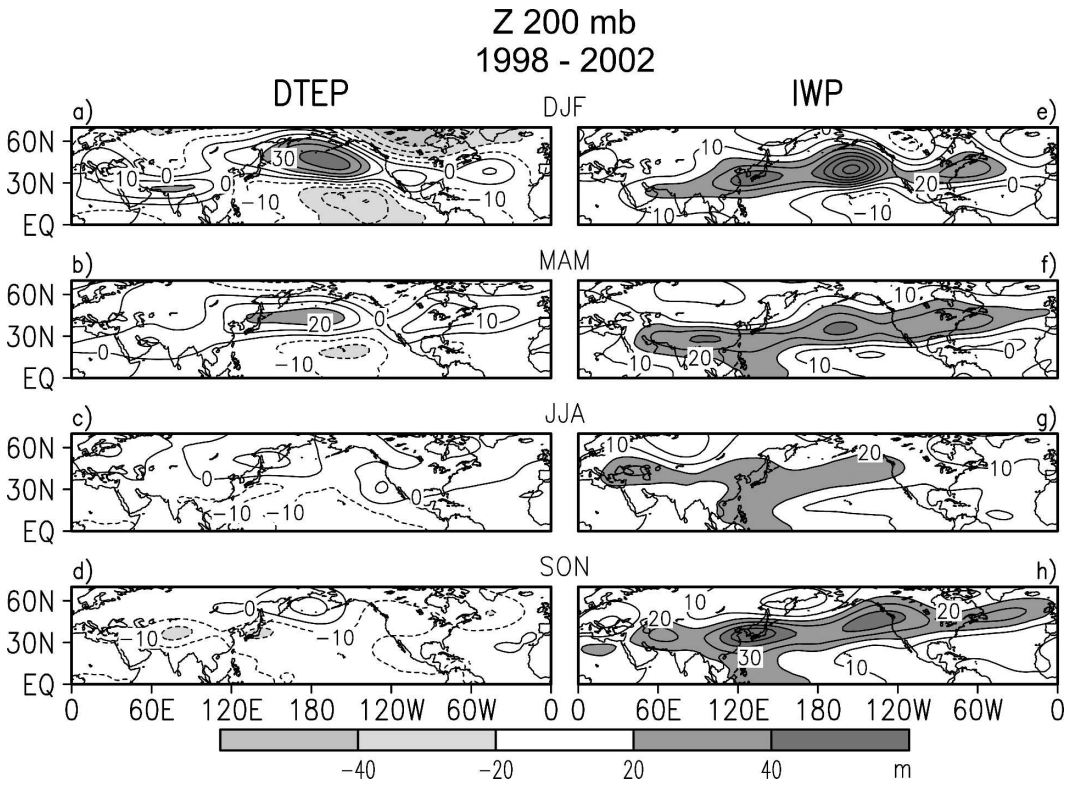

FIG. 3. Horizontal distributions of 200-mb height anomaly in the Northern Hemisphere, as obtained by averaging data for the calendar seasons of (a), (e) December–February, (b), (f) March–May, (c), (g) June–August, and (d), (h) September–November in subperiod 2. Results for the DTEP and IWP experiments are shown in (a)–(d) and (e)–(h), respectively. Contour interval: 10 m.

0.79 and 0.61, respectively.[1] Summation of the anomalies produced in the IWP and DTEP experiments yields a pattern (not shown) that exhibits an even higher spatial correlation (0.91) with the GLOBAL result. Hence, to first approximation, the total response in the GLOBAL experiment may be viewed as the linear sum of the responses to the forcings in the IWP and DTEP sectors, with the contribution of the IWP region being relatively stronger. The validity of this linear approximation has also been tested by a suite of SST anomaly experiments in which composite ENSO cycles in DTEP and the secular warming trend in IWP were prescribed separately, as well as in combination with each other. These model results (not shown) confirm that the response to SST forcings inserted in both DTEP and IWP bears a strong resemblance to the sum of the individual responses to the oceanic changes in the DTEP and IWP sectors.

The dependence of the Northern Hemispheric portion of the patterns in Figs. 2c,d on the phase of the annual cycle is illustrated in Fig. 3, which shows the 4-yr averages of the anomalies for various calendar seasons. These seasonal patterns indicate that the atmospheric responses to DTEP forcing are strongest in the boreal winter (Fig. 3a), during which the signals in the North Pacific–North American sector acquire a more wavelike appearance than is indicated in Fig. 2c. The anomalous ridge in the northern extratropics as simulated in the DTEP experiment exhibits a stronger zonal symmetry in boreal spring (Fig. 3b). The amplitude of this springtime anomaly is much reduced in the summer and fall seasons (Figs. 3c,d). On the contrary, the extended ridge in the northern midlatitude zone is a robust feature in the IWP experiment through the boreal fall, winter, and spring (Figs. 3h,e,f), and is somewhat reduced in summer (Fig. 3g). The notable disparity between the seasonal dependence of the midlatitude responses to IWP and DTEP forcing suggests that different processes may be at work in linking the SST anomalies in these two sectors to the extratropical atmosphere. The contrast between the wavelike response to ENSO-related forcing in boreal winter (Fig. 3a) and

[1] These spatial correlation coefficients have been computed using departures of local values from the areal average.

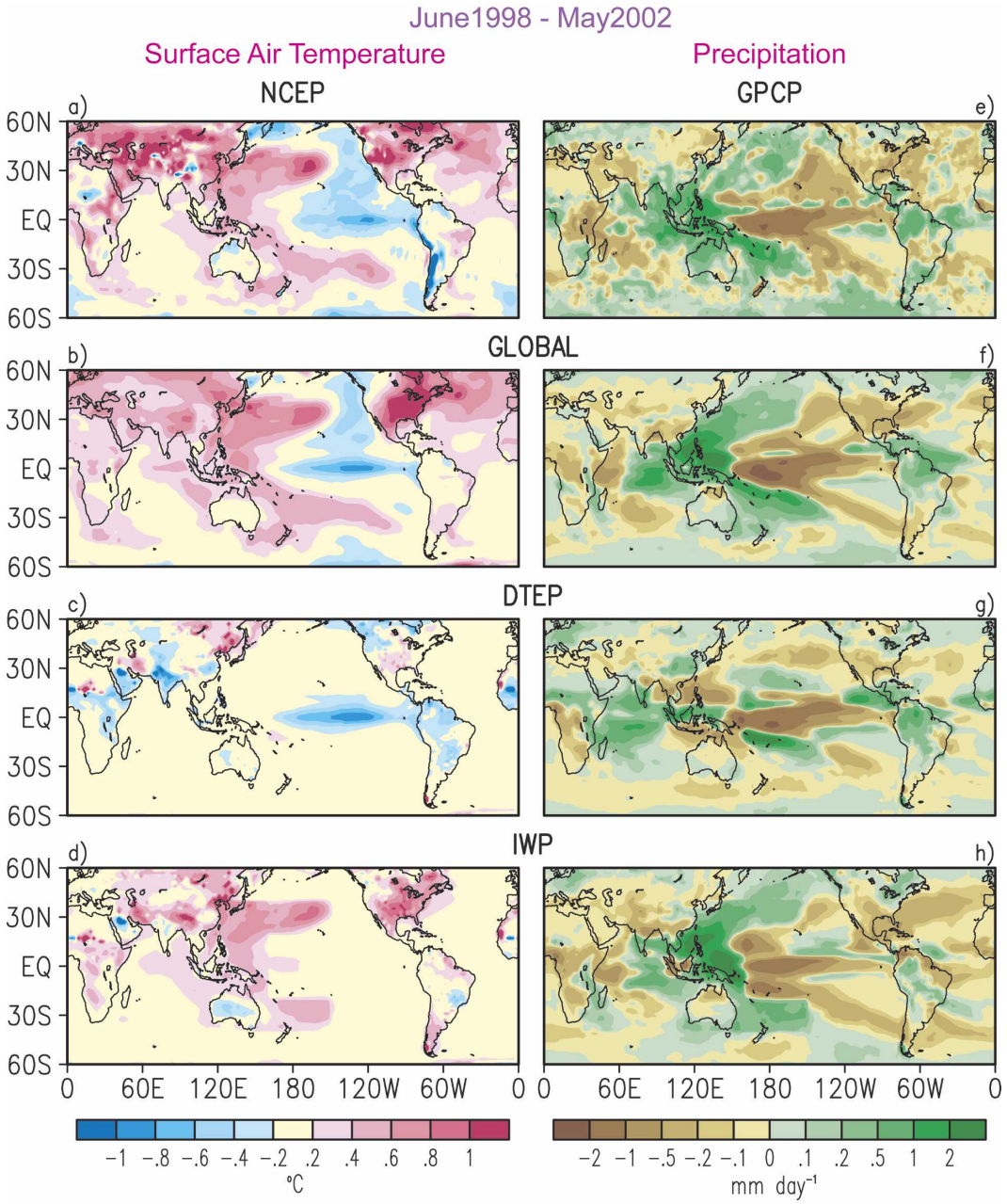

FIG. 4. Same as in Fig. 2, but for anomalies of (a)–(d) surface air temperature and (e)–(h) precipitation. Observational estimates are shown in (a), (e). Results in the remaining panels are based on (b), (f) GLOBAL, (c), (g) DTEP, and (d), (h) IWP experiments.

the zonally symmetric response to SST anomaly in the IWP sector during summer (Fig. 3g) may contribute to the seasonal dependence of variability and predictability, as noted by Schubert et al. (2002) and Kumar et al. (2003).

The observed and model-simulated anomalies of surface air temperature and precipitation in subperiod 2 are presented in Figs. 4a–d and 4e–h, respectively. As noted by Hoerling and Kumar (2003), abnormal warmth and dryness were observed over many land areas in the northern subtropics and extratropics during this period (Figs. 4a,e). The patterns in the tropical Pacific are typical of La Niña conditions (Ropelewski and Halpert 1989), with temperature and precipitation being below normal in the central and eastern portions of that basin, and above normal near its western bound-

ary. Wet anomalies occurred over the near-equatorial Atlantic and eastern Indian Oceans, as well as over tropical South America, whereas dryness prevailed over eastern tropical Africa and the western Indian Ocean. Many of the above features are discernible in the corresponding patterns simulated in the GLOBAL (Figs. 4b,f) and IWP (Figs. 4d,h) experiments, thus indicating the dominant role of the SST anomalies in the IWP region in forcing the worldwide temperature and precipitation anomalies in the modeled and observed atmospheres. The simulated response in the DTEP experiment (Figs. 4c,g) bears a considerable resemblance to the observed patterns in most parts of the tropical Pacific and South America. However, the results from the DTEP experiment are notably different from the observations as well as the GLOBAL and IWP simulations over the northwestern subtropical Pacific, as well as eastern tropical Africa and the nearby waters. The warm and dry anomalies over southwestern Asia and much of the United States are much more evident in the GLOBAL and IWP runs than in the DTEP experiment.

The model responses displayed in Figs. 2 and 4 are based on ensemble averages over all individual runs for each experiment. To gain an appreciation of the range of responses in a given ensemble, the anomaly value for each member of the ensemble has been rank ordered according to its magnitude, and the values corresponding to specific percentiles of the population were then determined. This procedure has been performed for the averages over the June 1998–May 2002 period. At each longitude along a selected zonal belt, an average of the values was taken over the meridional width of that belt prior to the rank-ordering step. The north–south extent of the belt is 30°–50°N for 200-mb height, and 20°–40°N for surface air temperature and precipitation. These choices are guided by the latitudinal positions of the principal model anomalies appearing in Figs. 2 and 4. The results of this analysis are presented in Fig. 5, for 20 members of the GLOBAL experiments (top row), and 30 members each of the DTEP (middle row) and IWP (bottom row) experiments. For each variable in each experiment, the longitudinal dependence of the values corresponding to the 50th percentile (i.e., the median) is indicated by a curve; the range between the 25th and 75th percentiles are depicted by dark shading, whereas the 10th–25th and 75th–90th ranges are denoted by light shading.

For the 200-mb height field (left panel in Fig. 5), almost all of the individual members of the GLOBAL and IWP experiments produce positive anomalies around the entire latitude belt. The range of the responses in individual members of these two experiments (as illustrated by the vertical extent of the shading at a given longitude) is generally smaller than the overall signal strength (as approximated by the departure of the median curve from the abscissa). These results provide strong evidence on the reproducibility of the patterns in Figs. 2b,d in individual runs of the GLOBAL and IWP experiments. On the contrary, the sampling fluctuations among individual members are much larger in comparison to the amplitude of the median anomaly in the DTEP experiment, thus yielding much smaller signal-to-noise ratios in most longitudes. For surface air temperature (middle panel in Fig. 5), a large majority of the members of the GLOBAL experiment produce warm anomalies in the North American and Eurasian sectors. Reproducible warm responses are also generated in the IWP runs over North America and some portions of Eurasia. The temperature response in the DTEP experiment is relatively much weaker over the oceanic areas, primarily due to the absence of any anomalous SST forcing within the 20°–40°N zone in that experiment. The DTEP result also shows less robust warming over North America and Eurasia. The precipitation statistics (right panel in Fig. 5) for the GLOBAL and IWP experiments bear a considerable resemblance to each other, with most ensemble members producing dry anomalies over North America and much of Eurasia. The corresponding responses in DTEP are relatively noisier.

b. 1997–98 and 2002–03 subperiods

The patterns of 200-mb height anomalies for subperiods 1 and 3 are presented for NCEP–NCAR reanalysis data (Figs. 6a,e) and model simulation in the GLOBAL (Figs. 6b,f), DTEP (Figs. 6c,g), and IWP (Figs. 6d,h) experiments. The left and right panels in each row of this figure share rather common large-scale characteristics, with the amplitudes in subperiod 1 being generally higher than those in subperiod 3. The results for both the observations and the GLOBAL simulation are indicative of equator-wide positive height anomalies, and zonally extended negative anomalies in the northern and southern extratropics. The negative height anomalies are even more evident in the DTEP simulation (Figs. 6c,g). On the other hand, the SST forcing in IWP (Figs. 6d,h) produces mostly anomalous ridges in midlatitudes. Comparison among the various model panels in Fig. 6 reveals that the atmospheric patterns in the GLOBAL experiment are dominated by the response to the El Niño events in the DTEP sector during the two subperiods considered here. These responses more than compensate for the opposing, but relatively weaker, anomalies associated with the warm SST forcing in IWP.

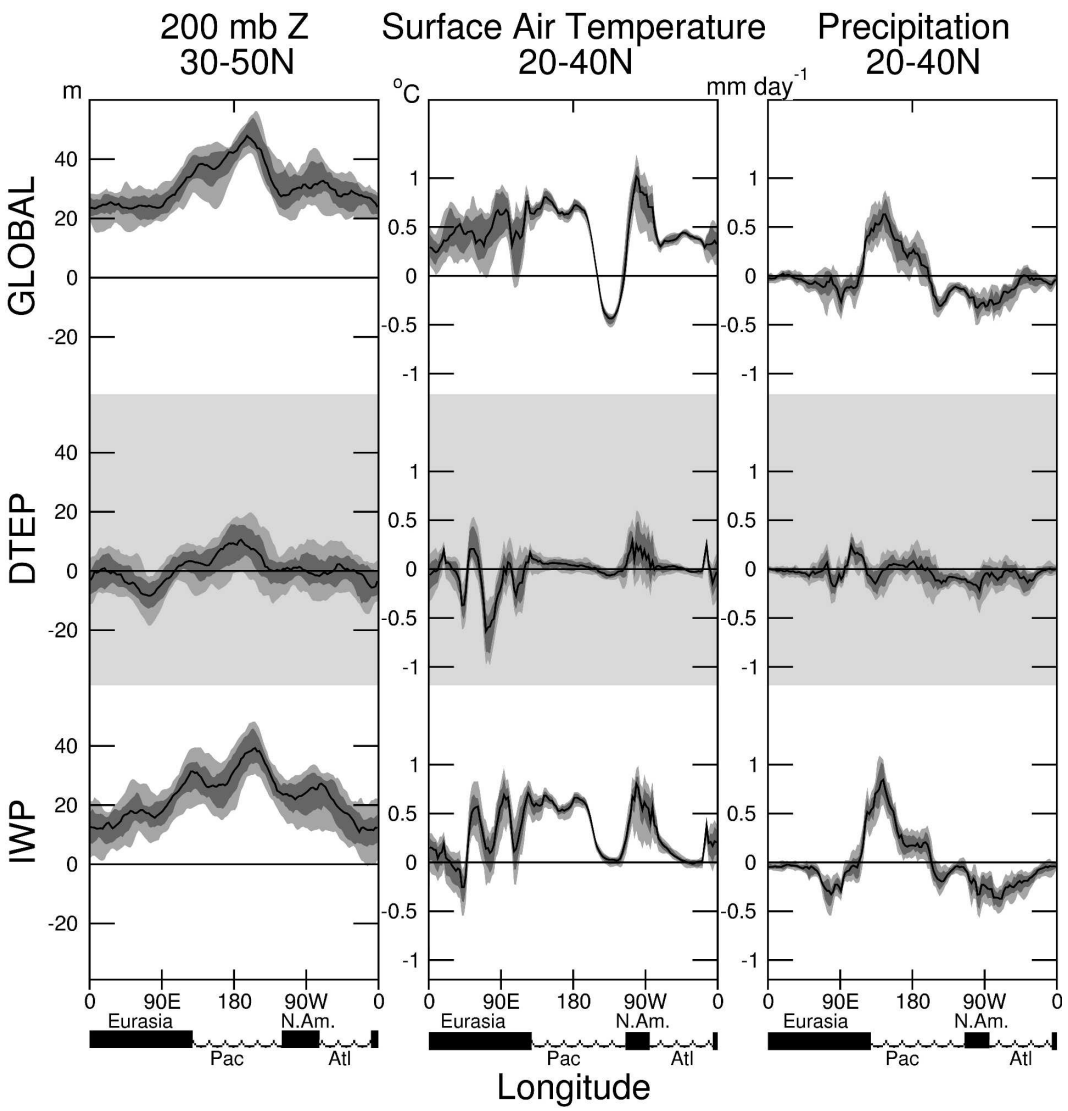

FIG. 5. Longitudinal distributions of the percentile values in the population of anomalies simulated in individual members of the (top) GLOBAL, (middle) DTEP, and (bottom) IWP experiments, for (left) 200-mb height averaged between 30° and 50°N, and (middle) surface air temperature and (right) precipitation, both averaged between 20° and 40°N. Results are based on averages over subperiod 2. The 50th percentile values are indicated by the black curves. The 25th–75th percentile range is depicted using dark shading. The 10th–25th and 75th–90th percentile ranges are represented by light shading.

It is also of interest to contrast the patterns in Fig. 6 with those in Fig. 2 for subperiod 2. The DTEP results in the two figures have opposite polarities, reflecting the differing responses to El Niño and La Niña conditions; whereas the persistent warm SST anomaly in IWP yields essentially the same atmospheric pattern throughout the three subperiods. The extratropical signals accompanying the DTEP and IWP forcings are mostly in phase in subperiod 2, but are out of phase in subperiods 1 and 3.

For subperiods 1 and 3, the spatial correlation coefficients between the 200-mb height response in the GLOBAL experiment and the linear sum of the responses in the DTEP and IWP experiments are higher than the correlations between the GLOBAL and DTEP patterns, or between the GLOBAL and IWP patterns. Moreover, addition of the DTEP and IWP patterns leads to substantial reduction of the rms differences from the GLOBAL pattern (by as much as a factor of 2–3), as compared to the results based on matching the GLOBAL pattern with each of the DTEP or IWP patterns separately. In accord with the findings

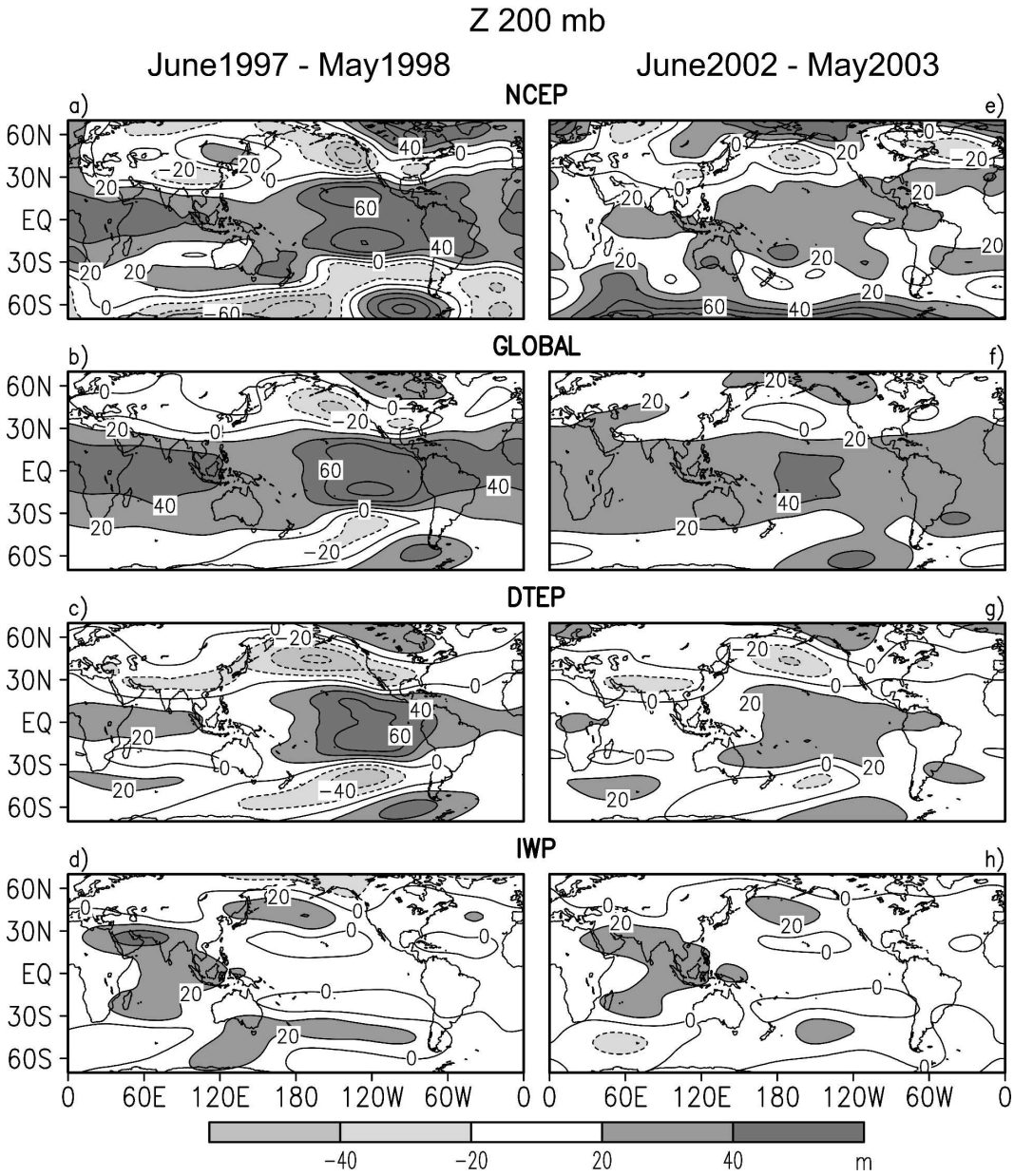

FIG. 6. Same as in Fig. 2, but for (a)–(d) June 1997–May 1998 (subperiod 1) and (e)–(h) June 2002–May 2003 (subperiod 3).

for subperiod 2, the signals in GLOBAL may be viewed as the linear combination of the responses to the SST forcings in the DTEP and IWP sectors.

c. *Evolution of zonal averages through all subperiods*

The temporal development through the 1997–2004 period of the zonally elongated features in Figs. 2 and 6 is depicted in greater detail in Fig. 7. The latter diagram contains the time–latitude distributions of the zonal averages of 200-mb height anomalies, as computed using monthly means of (Fig. 7a) NCEP–NCAR reanalyses, and output from the (Fig. 7b) GLOBAL, (Fig. 7c) DTEP, and (Fig. 7d) IWP experiments. The near-equatorial evolution in the observed pattern (Fig. 7a) consists of three main stages: strong positive anomalies from early 1997 to late 1998, negative anomalies from 1999 to early 2001, and positive anomalies thereafter. This succession corresponds closely with the concurrent evolution of El Niño and La Niña events. In the extratropics, the observations show an anomalous trough

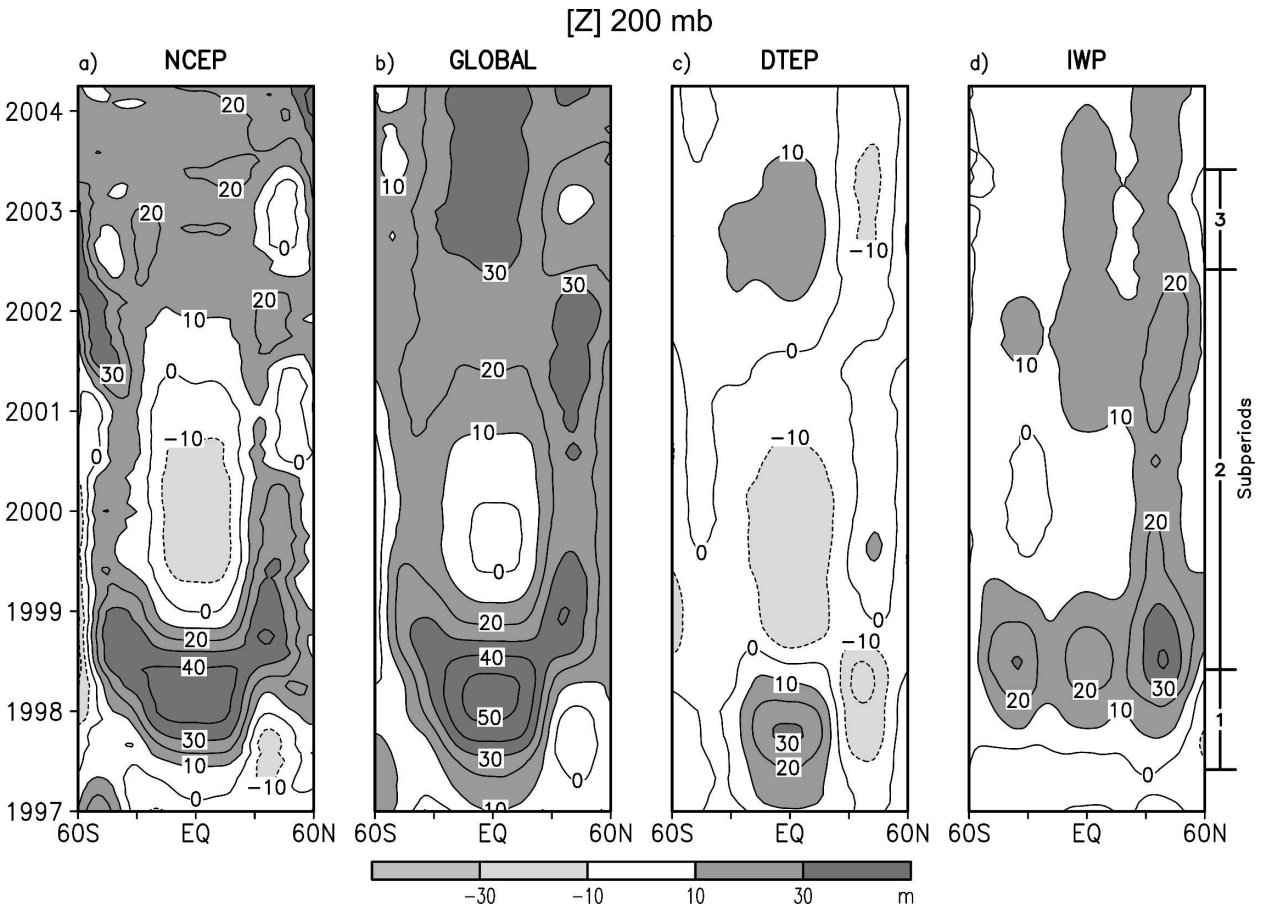

FIG. 7. Time–latitude distributions of anomalies of zonally averaged height at 200 mb, as obtained from (a) NCEP–NCAR reanalyses, and model simulations in the (b) GLOBAL, (c) DTEP, and (d) IWP experiments. A 13-month running-mean smoothing has been applied. Contour interval: 10 m. The span of subperiods 1, 2, and 3 is indicated along the right margin of the right panel.

centered at 40°N in 1997, followed by a pair of anomalous ridges near 45°N and 45°S that persisted through a large portion of the period from 1998 to early 2002. Most of the above observed signals are well captured in the GLOBAL experiment (Fig. 7b). The strength and duration of the negative equatorial anomaly in 1999–2000 are considerably reduced in the simulation as compared with the NCEP–NCAR result. The positive tropical anomaly in 2002–04 is much stronger in the GLOBAL experiment than in the observed pattern.

In the DTEP simulation (Fig. 7c), the El Niño years are associated with positive height anomalies in the Tropics and negative anomalies in the northern extratropics. The signs of these anomalies are reversed in the La Niña years. The continued warmth in the SST field within IWP leads to above-normal heights in the equatorial zone as well as the midlatitude belts of both hemispheres through much of the 1998–2003 period (Fig. 7d). Enhanced positive height anomalies are generated in the IWP runs near the equator in the termination stages of the 1997–98 and 2002–03 El Niño events. This protraction of the tropical height changes due to forcing from the IWP sector is in accord with the findings of Kumar and Hoerling (2003). The extratropical height anomalies in the DTEP and IWP experiments tend to be in phase (out of phase) during La Niña (El Niño) years. The linear sum of the patterns in Figs. 7c,d (not shown) bears a strong similarity to that in Fig. 7b.

The extent to which the principal features in Fig. 7 can be reproduced in individual members of the ensemble experiments has been assessed by a procedure similar to that used in constructing Fig. 5. In the present application, the zonal-mean 200-mb height anomalies at a given latitude were rank ordered, so as to determine the values corresponding to various percentiles. The analysis was performed using time averages for each of the two El Niño periods June 1997–May 1998 (subperiod 1) and June 2002–May 2003 (subperiod 3), as well as the extended La Niña period June 1998–May 2001 (a shortened version of subperiod 2, with preva-

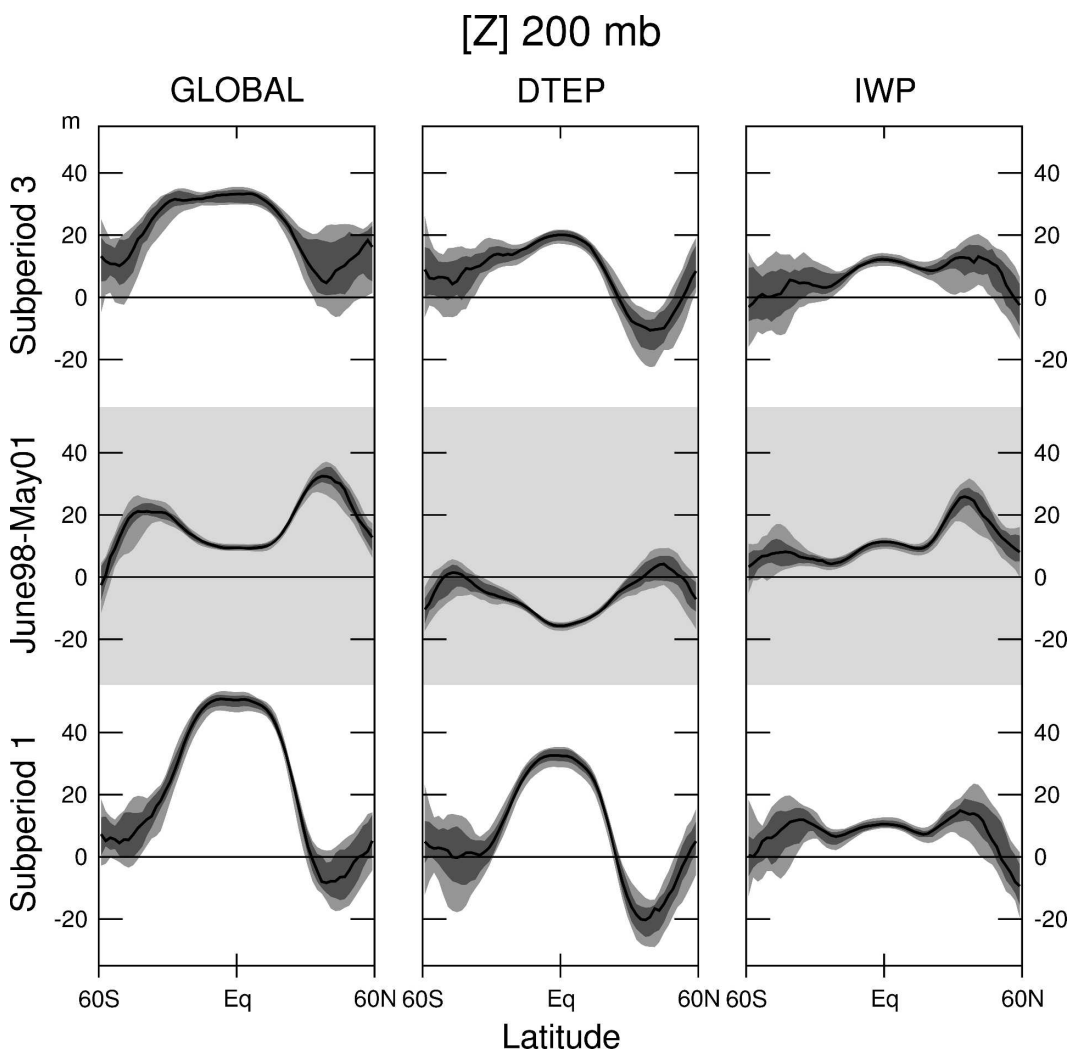

FIG. 8. Latitudinal distributions of the percentile values in the population of anomalies simulated in individual members of the (left) GLOBAL, (middle) DTEP, and (right) IWP experiments, for zonal means of 200-mb height averaged over (top) subperiod 3, (middle) June 1998–May 2001, and (bottom) subperiod 1. The 50th percentile values are indicated by the black curves. The 25th–75th percentile range is depicted using dark shading. The 10th–25th and 75th–90th percentile ranges are represented by light shading.

lent cold SST anomalies throughout the DTEP region). The latitudinal dependence of the percentile values thus obtained is illustrated in Fig. 8 by using the same convention as in Fig. 5. In the tropical zone, the responses in individual members tend to stay within a narrow range about the median, thus indicating a high degree of reproducibility of the tropical signals in all experiments and during all periods considered here. Despite the notable increase in intersample variability at higher latitudes, the strength of following extratropical signals is seen to stand well above the spread among individual members: the anomalous ridges near 45°N and 45°S during the June 1998–May 2001 period in the GLOBAL panel, the anomalous troughs near 45°N in subperiods 1 and 3 in the DTEP panel, and the anomalous ridges near 45°N in all three periods in the IWP panel.

4. Simulated atmospheric responses in earlier anomalous SST episodes

In analogy to the 1997–2003 period, several episodes in earlier decades are also characterized by prominent El Niño and La Niña events in the DTEP sector, and concurrently by notable SST changes in IWP. Two such examples are presented in Fig. 9, which shows the anomalous SST evolution in 1953–58 and 1972–77 by using a format similar to Fig. 1a. The right panels in

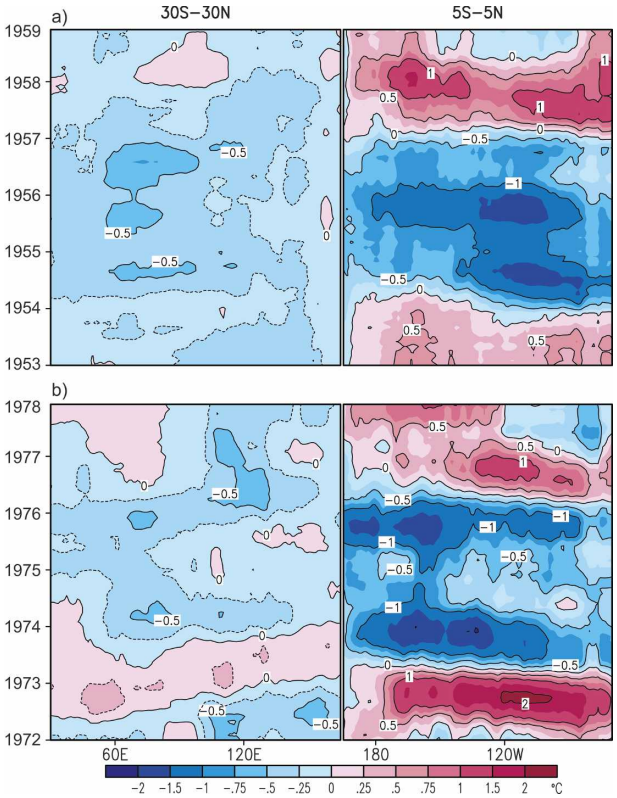

FIG. 9. Same as in Fig. 1a, but for the (a) 1953–58 and (b) 1972–77 periods.

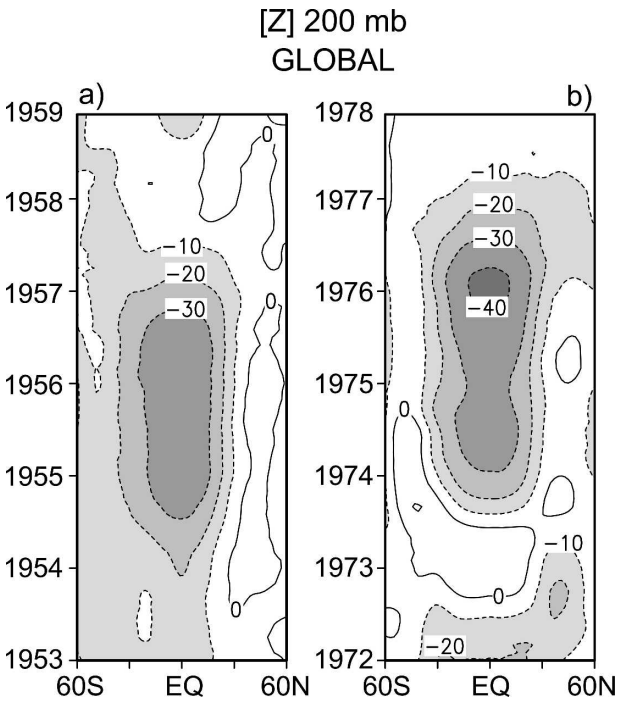

FIG. 10. Same as in Fig. 7b, but for the (a) 1953–58 and (b) 1972–77 periods.

Fig. 9 indicate the occurrence of El Niños in 1953, 1957, 1972, and 1976, as well as the protracted La Niñas of 1954–56 and 1973–75. The left panels in Fig. 9 reveals that, in contrast to the above-normal SST in IWP during 1997–2003, cold conditions prevailed in the same region in 1954–56 and 1974–75.

The results for the 1998–2002 period indicate that the extratropical atmospheric response to warm SST anomalies in IWP during 1998–2002 tends to reinforce the response to concurrent cold SST anomalies in DTEP; whereas tropical responses to the SST changes in the two regions tend to oppose each other. These findings may be contrasted with Fig. 10, which shows zonally averaged anomalies of 200-mb height, as simulated in the GLOBAL experiment for the 1953–58 and 1972–77 periods. The tropical zone in these charts is dominated by the negative height anomalies extending from 1954 to 1956 and from 1974 to 1976. These features are much stronger than that simulated in 1998–2002 (Fig. 7b). On the other hand, the extratropical anomalous ridges in Fig. 10 are considerably weaker than those in Fig. 7b. The results in Fig. 10 illustrate that the cold conditions in IWP and DTEP yield in-phase responses in the Tropics, and out-of-phase responses in midlatitudes (thus accounting for the weak extratropical signals). The corresponding distributions based on NCEP–NCAR reanalyses for 1954–56 and 1974–76 (not shown) also indicate robust negative height anomalies in the Tropics and feeble positive anomalies in the extratropics.

5. Implications on North American surface climate

The differences between the extratropical 200-mb responses in various periods of interest, as pointed out in the previous sections, could exert considerable influences on the near-surface climate in North America. The distributions of the anomalous surface air temperature and precipitation in this region, as simulated in the GLOBAL experiment, are presented in the left panels of Fig. 11 for the periods of January 1954–December 1956, January 1974–December 1975, and June 1998–May 2002 (subperiod 2). The corresponding observational results are shown in the right panels of Fig. 11 using NCEP–NCAR reanalyses for the temperature field, as well as precipitation datasets of Dai et al. (1997; based on station records for the 1954–56 and 1974–75 periods) and GPCP (for 1998–2002). The eastward extension of the prominent midlatitude ridge to the Western Hemisphere in the GLOBAL experiment during subperiod 2 (see Fig. 2b) is seen to be accompanied by

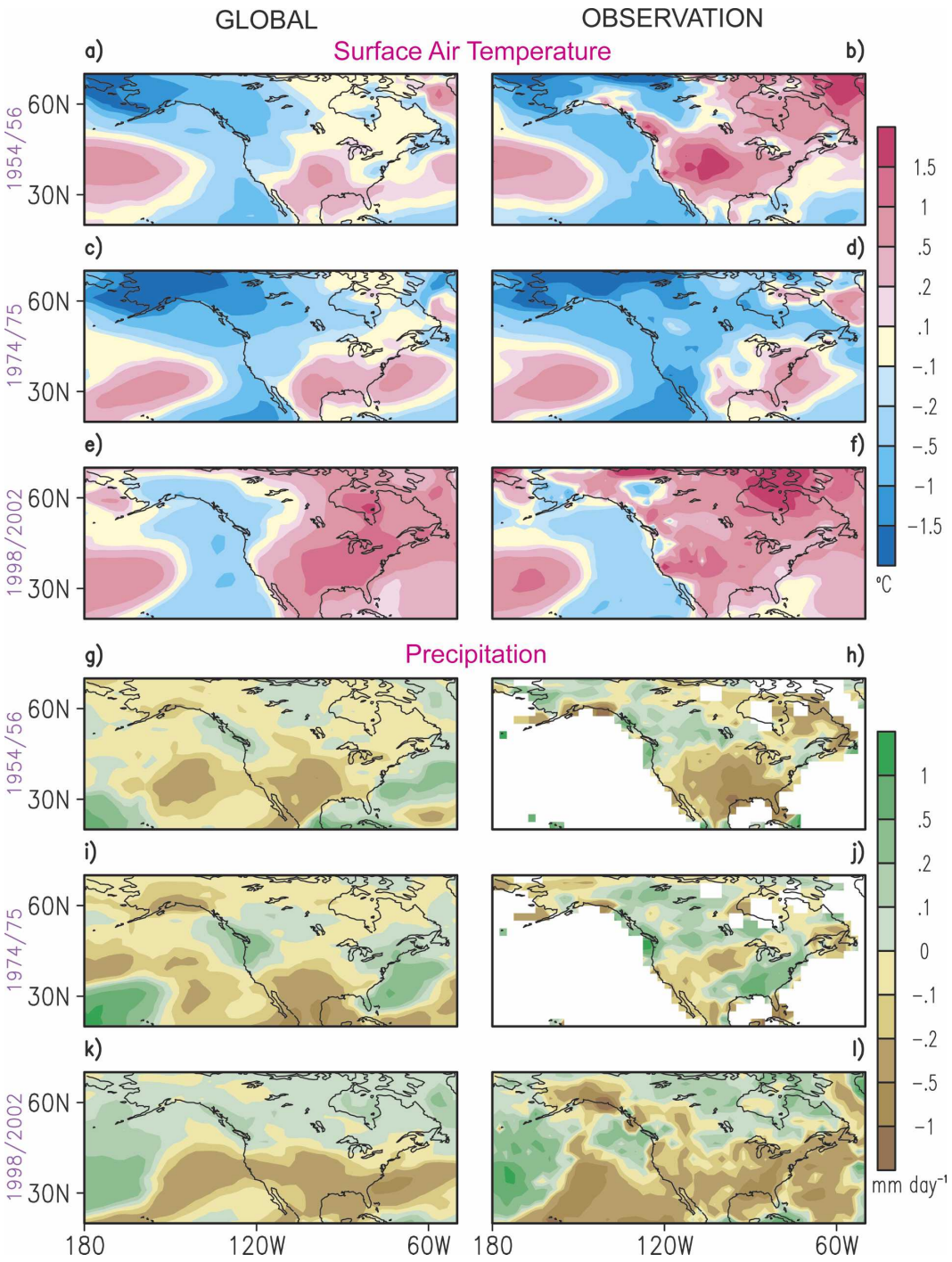

FIG. 11. Horizontal distributions in the North American sector of the anomalies of (a)–(f) surface air temperature and (g)–(l) precipitation, for the (a), (b), (g), (h) January 1954–December 1956; (c), (d), (i), (j) January 1974–December 1975; and (e), (f), (k), (l) June 1998–May 2002 periods. Results from the GLOBAL experiment (observational datasets) are shown in the left (right) panels.

warm surface temperature anomalies over a large fraction of the North American landmass (Fig. 11e), and by dry anomalies along a wide zone extending from 160° to 50°W and centered near 35°N (Fig. 11k). Due to opposing effects of the SST forcings in IWP and DTEP during 1954–56 and 1974–75 (see arguments in previous sections), the simulated anomalous ridge over North America is much weaker and less organized in those

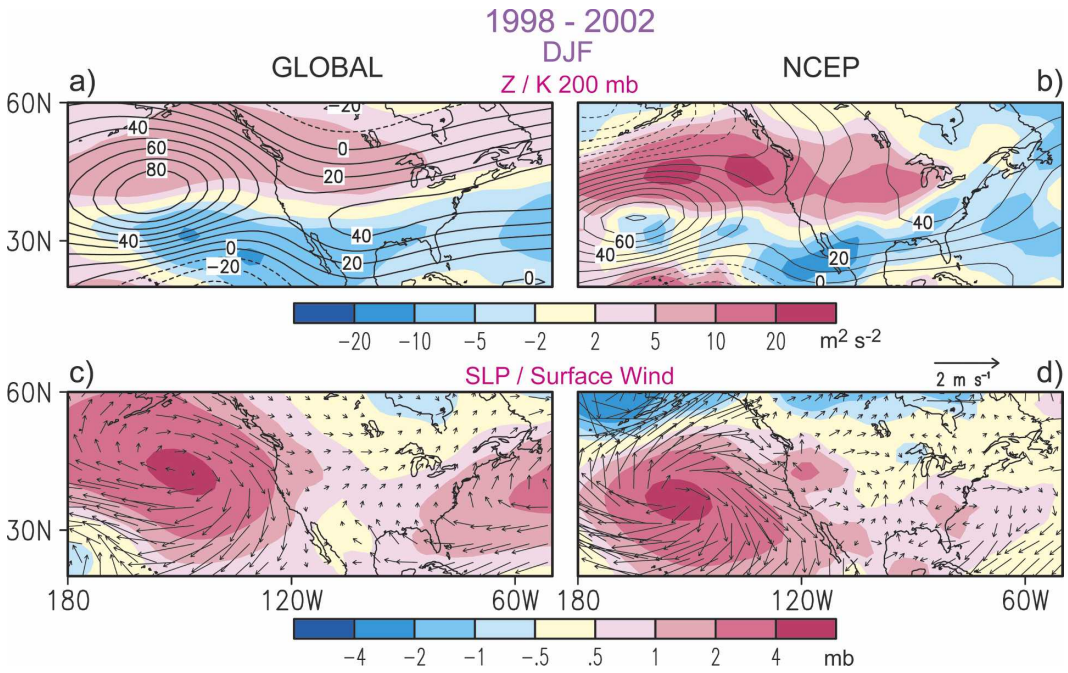

FIG. 12. Horizontal distributions in the North American sector of the anomalies of (a), (b) 200-mb height (contours, interval: 10 m) and transient eddy kinetic energy K (shading, see scale bar at bottom), and (c), (d) sea level pressure (shading, see scale at bottom) and surface wind vector (arrows, see scale at upper right). Results from the GLOBAL experiment (observational datasets) are shown in left (right) panels, and are based on averages over the four December–February seasons in the 1998–2002 period.

earlier periods (not shown). The amplitude or spatial coverage of the corresponding temperature and precipitation changes (Figs. 11a,c,g,i) are relatively less than those simulated in subperiod 2.

The model and observed features in subperiod 2 (Figs. 11e,f,k,l) are in fair agreement with each other, with the exception of the discrepancies near the Gulf of Alaska. The observations also indicate anomalously warm and dry conditions in 1954–56, which are discernible in the simulation, although the model underestimates the spatial extent of the warm anomalies (Figs. 11a,b,g,h). For the 1974–75 period, cold conditions prevail over western and northwestern North America in both the observed and simulated temperature patterns (Figs. 11c,d). The correspondence between the precipitation anomalies in the model simulation and observation for this period is relatively weaker (Figs. 11i,j).

The seasonal dependence of the precipitation and temperature anomalies in subperiod 2 has been examined by partitioning the data within 1998–2002 according to the four conventional seasons (December–February, March–May, etc.), and then plotting the counterparts of Figs. 11e,f,k,l for each of these seasons. The results based on both observations and output from the GLOBAL experiment (not shown) indicate that the precipitation and temperature signals are strongest in the vicinity of the continental United States during the boreal winter. The circulation features accompanying such changes are illustrated in Fig. 12, which shows the anomalous wintertime distributions of (Figs. 12a,b) 200-mb height (contours), and eddy kinetic energy K based on time-filtered wind data with periods between 2–10 days being retained, and (Figs. 12c,d) sea level pressure (SLP, shading) and surface wind vector (arrows). All patterns are based on averages over the four winter seasons (December–February) in the 1998–2002 period. Model and observational data are presented in Figs. 12a,c and 12b,d, respectively.

As mentioned earlier, the model pattern for 200-mb height (contours in Fig. 12a) is dominated by a belt of positive anomaly extending from the North Pacific across the continental United States to the North Atlantic. The enhanced eastward flows north of this anomaly are coincident with above-normal transient eddy activities, as may be inferred from the positive changes in K (shading in Fig. 12a) along the 40°–60°N belt. Conversely, the level of synoptic-scale variability is suppressed to the south of the anomalous ridge, when the strength of the zonal flow is reduced. There exists a strong spatial correspondence between the wintertime patterns of K (Fig. 12a) and precipitation (not shown,

but similar to Fig. 11k), with the weakened weather disturbances along the southern United States and northern Mexico being associated with below-normal precipitation over that region. Near the sea level, anticyclonic anomalies are simulated in the midlatitude North Pacific and North Atlantic (Fig. 12c). These surface features are situated beneath the positive height anomalies at 200 mb (Fig. 12a), thus implying an equivalent barotropic structure for the atmospheric changes over oceanic areas. The strong positive SLP anomaly over the North Pacific serves to block the passage of winter storms to the southern portion of North America, hence contributing to the dry conditions in that region. The warm southerly flows on the western flank of the Atlantic anticyclone anomaly partially accounts for the above-normal temperatures over the eastern and central United States (see Fig. 11e).

Some agreements are discernible between the simulated and observed patterns in Fig. 12 over the midlatitude North Pacific, where both the NCEP–NCAR reanalyses and the GLOBAL experiment indicate the presence of an anomalous anticyclone throughout the troposphere. The NCEP–NCAR data also support a northward shift in the track of storm activity in the North Pacific–North American sector (shading in Fig. 12b). The simulated 200-mb height anomaly over eastern United States–North Atlantic, as well as the attendant near-surface circulation anomalies, are much less evident in the NCEP–NCAR patterns.

6. Generation of zonally symmetric features by eddy–mean flow interaction

a. Geographical considerations

As is evident from Figs. 12a,b, variations in the seasonally averaged circulation exert considerable influences on the behavior of synoptic-scale disturbances, which could in turn feed back to the ambient low-frequency flow pattern through eddy transports of momentum and heat. To evaluate the contribution of transient eddy forcing to the zonally elongated features seen in the model patterns in Figs. 2b–d, the analysis procedure described in L05 has been applied to the output from the three individual experiments for subperiod 2. Daily data of the horizontal wind components u, v at 200 mb were time filtered to retain synoptic-scale fluctuations with periods of 2–10 days. Monthly statistics $\overline{u'u'}$, $\overline{v'v'}$, and $\overline{v'u'}$ were calculated, where the overbar and prime represent monthly average and deviation from monthly average, respectively. Ensemble means of these quantities over subperiod 2 were evaluated for each experiment. Two indicators of eddy behavior and feedback were then computed: the extended

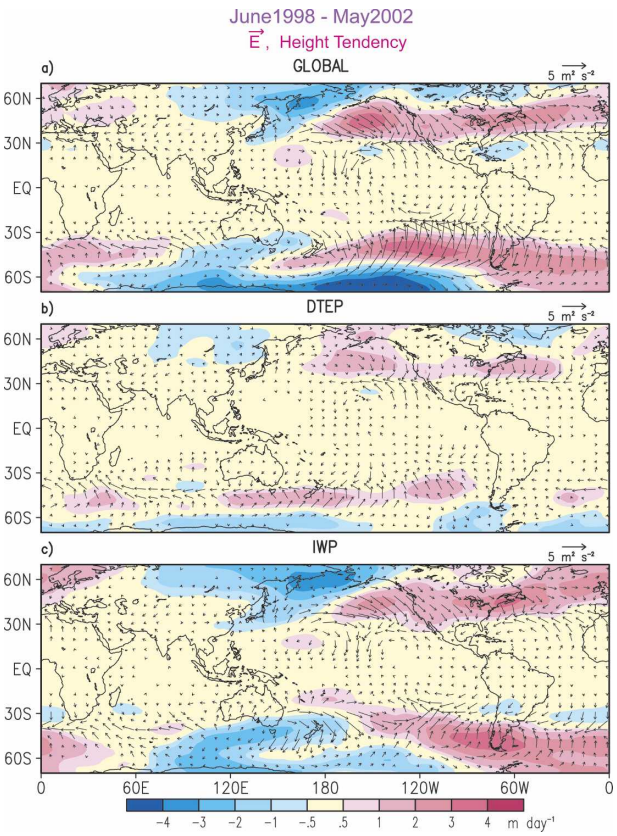

FIG. 13. Horizontal distributions of 200-mb anomalies of extended Eliassen–Palm vectors **E** (arrows, see scale at upper right) and eddy-induced height tendencies (shading, see scale bar at bottom) for June 1998–May 2002 (subperiod 2), as obtained from model simulations in the (a) GLOBAL, (b) DTEP, and (c) IWP experiments. All variance and covariance statistics have been computed using 2–10-day filtered data.

Eliassen–Palm vector as formulated by Trenberth (1986) $\mathbf{E} = (\overline{v'v'} - \overline{u'u'})/2\mathbf{i} - \overline{v'u'}\mathbf{j}$, and the height tendency induced by the barotropic component of the transient eddy forcing $\partial z/\partial t = (f/g)\nabla^{-2}\pi$. Here z is the geopotential height, f is the Coriolis parameter, g is the gravitational acceleration, and π is the convergence of eddy vorticity fluxes, which may be expressed in terms of $\overline{u'u'}$, $\overline{v'v'}$, and $\overline{v'u'}$ [e.g., see Eq. (2) in Lau (1988)]. The zonal wind acceleration and the geopotential height tendency resulting from eddy momentum transports may be inferred from the divergence of **E** and the pattern of $\partial z/\partial t$, respectively. The departure from climatology of the distributions of **E** (arrows) and $\partial z/\partial t$ (shading) for subperiod 2 are presented in Fig. 13. Results are shown using eddy statistics from the (Fig. 13a) GLOBAL, (Fig. 13b) DTEP, and (Fig. 13c) IWP experiments.

In the DTEP experiment (Fig. 13b), the magnitudes of the **E** vectors and $\partial z/\partial t$ are largest in two zonal belts

in the extratropics: one extending eastward from the central North Pacific across North America to the western North Atlantic, and the other from south of Australia to the South Pacific. Within these elongated regions of enhanced eddy feedbacks, the anomalous **E** vectors are mostly directed equatorward, thus leading to convergence of **E** (zonal wind deceleration) on the equatorward flank of the zonal belts, and divergence of **E** (zonal wind acceleration) on the poleward flank. Positive values of $\partial z/\partial t$ prevail along the axes of the zonal belts. This configuration of wind and geopotential height tendencies is consistent with geostrophy. The spatial correspondence between the anomalous patterns of z (Fig. 2c) and $\partial z/\partial t$ (Fig. 13b) in the vicinity of the zonal belts suggests that the transient eddies contribute to the eastward spread of the positive height anomalies in those sites.

The patterns of **E** and $\partial z/\partial t$ in the IWP experiment (Fig. 13c), and their relationships with the mean height anomaly in subperiod 2 (Fig. 2d), are analogous to those discerned from the DTEP runs (Figs. 13b and 2c). The zonal wind and height tendencies induced by the transient eddies are most pronounced along a pair of extratropical zonal belts over the North America–North Atlantic and South America–South Atlantic sectors. The anomalous eddy activities lead to positive midlatitude height tendencies in much of the Western Hemisphere, where considerable similarities are discernible between the anomalous patterns of $\partial z/\partial t$ and z. The eddy-induced tendencies in the IWP result are generally larger than those simulated in the DTEP runs, so that the patterns of **E** and $\partial z/\partial t$ in the GLOBAL experiment (Fig. 13a) bear a stronger resemblance to those in the IWP simulation (Fig. 13c) than the DTEP experiment (Fig. 13b).

The mechanisms contributing to the formation of zonally symmetric ridges in the IWP experiment may be summarized as follows: As demonstrated by the stationary model solution for the atmospheric response to diabatic heating in the IWP region (e.g., Simmons 1982; Ting and Yu 1998; L05), the positive 200-mb height anomalies in the Eastern Hemisphere (Fig. 2d) may be attributed to SST forcing in the Indo-Pacific region. These height anomalies are accompanied by enhanced zonal flows on their poleward flanks (see Fig. 3a in L05), which are associated with more vigorous development of synoptic-scale extratropical disturbances. As these transient fluctuations propagate eastward and attain maturity in the Western Hemisphere, the pattern of eddy momentum transport is perturbed in the latter locations, which results in eastward extension of the anomalous ridges in the Asian and Indian Ocean sectors.

b. Zonal mean perspectives

We proceed to examine the role of eddy momentum transports in the evolution of the height anomalies seen in Fig. 7 in a zonal mean context. The time–latitude distributions of the following zonal mean quantities are shown in Fig. 14: 200-mb zonal wind $[u]$ (contours) and eddy kinetic energy $K = [\overline{u'u'} + \overline{v'v'}]/2$ (shading) in Figs. 14a,d,g; 200-mb northward eddy momentum flux ($[\overline{v'u'}]$; shading) and its divergence (DivMF = $\partial([\overline{v'u'}]\cos^2\phi)/a\cos^2\phi\,\partial\phi$; contours) in Figs. 14b,e,h; and 200-mb DivMF (contours) and 500-mb pressure velocity $[\omega]$ (shading) in Figs. 14c,f,i. Here ϕ is the latitude, a the earth radius, and the square brackets represent the zonal average over complete latitude circles. Results are presented for the GLOBAL (top row), DTEP (middle row), and IWP (bottom row) experiments.

1) IWP EXPERIMENT

The persistent warm SST anomalies prescribed in the IWP sector result in the enhancement of the meridional temperature gradient near 45°N and 45°S, and relaxation of this gradient in the subtropics. These changes in the meridional temperature profile are evident throughout the troposphere (results not shown). In accord with the thermal wind relationship, these changes in the zonal mean baroclinicity are accompanied by strengthened eastward winds in the extratropics, and weakened winds in the subtropics (contours in Fig. 14g). Such zonal wind variations in turn modulate the intensity of transient disturbances (as inferred from the pattern of K; see shading in Fig. 14g), with positive anomalies of K located at and slightly poleward of the zones of enhanced $[u]$, and vice versa. Steadiness of the SST forcing in IWP throughout the 1997–2003 period accounts for the temporal continuity of the $[u]$ and K signals in Fig. 14g.

Various observational, modeling, and theoretical studies (e.g., Blackmon et al. 1977; Frederiksen 1983; Held 1975; Vallis et al. 2004) have shown that regions of enhanced eddy activity are coincident with convergence of momentum flux $\overline{v'u'}$. This relationship is consistent with the results displayed in Figs. 14g,h: the prolonged positive anomaly of K centered at 50°N is accompanied by momentum flux convergence; whereas the weakened eddy activity near 30°N is coincident with momentum flux divergence. Analogous interrelated changes in K, $[\overline{v'u'}]$ and DivMF are also discernible in the Southern Hemisphere, albeit with less temporal continuity.

The arguments and diagnostics presented by Chang (1996), Seager et al. (2003) [see their Eqs. (3) and (5)] and L05 illustrate that variations in DivMF are linked to changes in the zonally averaged circulation on the

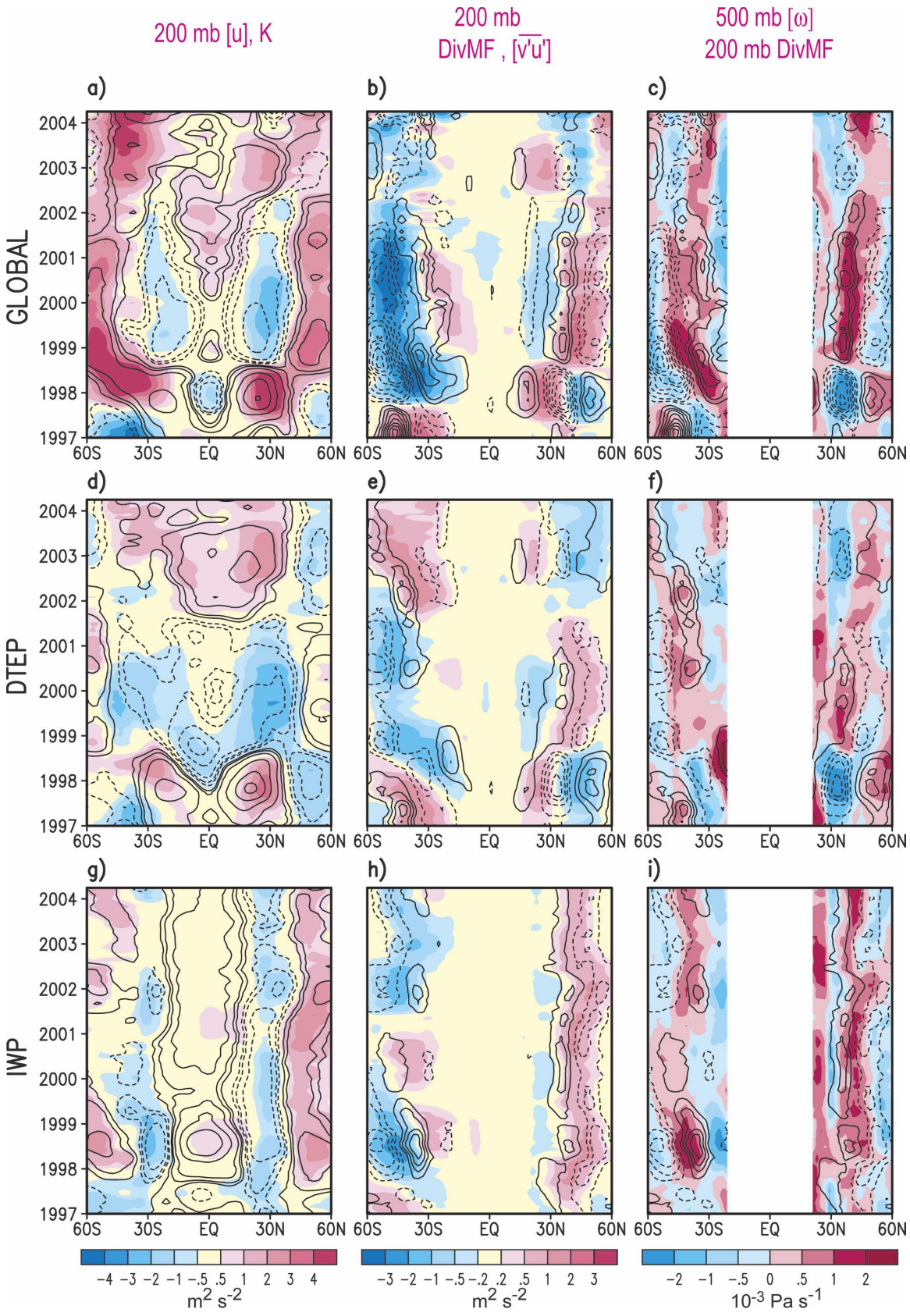
200 mb [u], K
200 mb
DivMF , [v'u']
500 mb [ω]
200 mb DivMF
a)
b)
c)
d)
e)
f)
g)
h)
i)
GLOBAL
DTEP
IWP
2004
2003
2002
2001
2000
1999
1998
1997
60S 30S EQ 30N 60N
−4 −3 −2 −1 −.5 .5 1 2 3 4
m2 s-2
−3 −2 −1 −.5 −.2 .2 .5 1 2 3
m2 s-2
−2 −1 −.5 0 .5 1 2
10-3 Pa s-1

meridional plane. Specifically, momentum flux divergence (DivMF > 0) is primarily balanced by the Coriolis torque associated with a poleward flow ($f[v] > 0$) at 200 mb, and vice versa. The eddy-induced changes of $[v]$ are in turn related to anomalies in the vertical component of the circulation through the continuity equation, with meridional convergence of $[v]$ at 200 mb corresponding to sinking ($[\omega] > 0$) in midtroposphere, and vice versa. The above relationships between DivMF and $[\omega]$ in the IWP experiment are substantiated by the results in Fig. 14i.[2] Of special interest is the prevalence of anomalous 500-mb sinking motion ($[\omega] > 0$) centered at 45°N. This zone is straddled by positive DivMF (which implies $[v] > 0$) to its south, and negative DivMF ($[v] < 0$) to its north. The enhanced subsidence simulated near 40°S is also flanked by similar (but less organized) signals of DivMF.

The adiabatic warming and cooling accompanying the eddy-induced vertical motion lead to changes in the temperature (and thickness) of the tropospheric column, and thereby influence the variability of the 200-mb height field. Comparison between the extratropical features of $[z]$ (Fig. 7d) and $[\omega]$ (Fig. 14i) confirms that warming due to the anomalous subsidence in midlatitudes is coincident with positive 200-mb height anomalies through much of the 1997–2003 period.

2) DTEP EXPERIMENT

The zonal mean statistics for the DTEP experiment, shown in the middle row of Fig. 14, exhibit a notable dependence on the evolution of El Niño and La Niña episodes. The relationships between the quantities displayed here during various subperiods may also be understood in terms of the processes delineated in the previous subsection. During the El Niño events in subperiods 1 and 3, the deep tropical heating produces equator-wide positive 200-mb anomalies (Figs. 6c,g). In the Eastern Hemisphere, the meridional width of this anomaly is generally narrower than that simulated in the IWP experiment (Figs. 6d,h), partially due to the limited north–south extent of the SST forcing in DTEP (mostly within 10° of latitude from the equator) as compared with that in IWP (as much as 40° from the equator). Accordingly, the enhanced zonal flows in the DTEP pattern (contours in Fig. 14d) are located close to the equator, at about 20°N and 20°S. These changes in $[u]$ are accompanied by enhanced eddy activity (see shading for K in Fig. 14d) and momentum flux convergence (contours in Fig. 14e) slightly farther poleward. The eddy-driven meridional circulation in subperiods 1 and 3 is hence characterized by divergence of $[v]$ and ascent at about 40°N and 40°S (Fig. 14f). The resulting adiabatic cooling is consistent with the negative 200-mb height anomalies simulated in these zones (Fig. 7c). The polarity of all of the above anomalies is reversed in the La Niña years in subperiod 2, with the eddy fluxes inducing subsidence and positive height anomalies in midlatitudes. Comparison between Figs. 14d–f and 14g–i indicates the effects of eddy feedbacks on the zonal mean flow are in phase in the DTEP and IWP experiments in subperiod 2. However, they are out of phase in subperiods 1 and 3, during which the signals corresponding to DTEP forcing are relatively stronger.

3) GLOBAL EXPERIMENT

Similar to other findings reported here, the results based on the GLOBAL experiment (Figs. 14a–c) may be viewed as the approximate linear superposition of the individual contributions from the IWP and DTEP runs. The cooperation between the eddy forcings in IWP and DTEP during subperiod 2 results in robust features in that interval. The correspondence between the GLOBAL and DTEP patterns in subperiods 1 and 3 reflects the dominance of the signals in DTEP over those in IWP with the opposite polarity.

7. Discussion

The evidence presented in this study illustrates the substantial role of the SST anomalies in the IWP sector

[2] Results in this panel (and in corresponding panels of GLOBAL and DTEP experiments) are shown only for latitudes poleward of 20°. Amplitudes of DivMF are generally weak in the Tropics (see Figs. 14b, e, h). Tropical features of $[\omega]$ are mostly governed by diabatic processes that are not directly related to the transient eddy forcing considered here.

←

FIG. 14. Time–latitude distributions of zonally averaged anomalies of (a), (d), (g) 200-mb zonal wind (contours, indicating values of ± 0.25, ± 0.5, ± 1, ± 2, ± 3 and ± 4 m s^{-1}) and transient eddy kinetic energy K (shading); (b), (e), (h) 200-mb transient eddy momentum flux $[\overline{v'u'}]$ (shading) and its divergence DivMF (contours, interval: 5×10^{-7} m s^{-2}); and (c), (f), (i) DivMF (contours, interval: 5×10^{-7} m s^{-2}) and 500-mb pressure velocity $[\omega]$ (shading). Results are shown for model simulations in (a)–(c) GLOBAL, (d)–(f) DTEP, and (g)–(i) IWP experiments. All variance and covariance statistics have been computed using 2–10-day filtered data. A 13-month running-mean smoothing has been applied to all quantities displayed here. Solid and dashed contours indicate positive and negative values, respectively. Zero contours are not plotted. Scale bars for the shading are displayed at the bottom of the respective column of the panels.

in the formation of zonally elongated height anomalies in the extratropics. The latter atmospheric features are particularly strong when the forcing in IWP is coincident with SST changes of the opposite polarity in DTEP, as occurred in 1998–2002. On the contrary, when the SST anomalies in IWP and DTEP are both above normal (e.g., subperiods 1 and 3) or both below normal (e.g., 1954–56 and 1973–75), the midlatitude responses to the forcings at the two oceanic sites tend to oppose each other.

The findings on the nature of local eddy–mean flow interactions (section 6a) are complementary to those deduced using zonal mean diagnostics (section 6b). In the latter approach, considerable simplification is achieved by ignoring longitudinal variations, and a direct link is identified between tropical SST forcing and the zonal mean component of the zonal wind, transient eddy momentum fluxes, eddy-induced circulation on the meridional plane, and the resulting geopotential height response in midlatitudes. By considering the zonal mean formulation, Seager et al. (2003) has proposed dynamical mechanisms that do not explicitly depend on zonal asymmetries, such as circulation patterns and transient eddy activity in specific geographical sites. The local analysis tools (such as the horizontal distributions of **E** and $\partial z/\partial t$) provide more detailed information that is not available from the zonal mean results. For instance, the patterns in Fig. 13 pinpoint the longitudinal sectors where the most active eddy feedbacks take place. Moreover, these local diagnostics allow us to associate such regions of enhanced eddy activity with the intensified quasi-stationary circulation farther upstream, which may in turn be linked to steady forcing due to the imposed SST anomaly. Conclusions obtained by averaging the local diagnostic results (such as in Fig. 13) along complete latitude circles are consistent with those drawn directly from the zonal mean framework (Fig. 14). The complementariness of these two approaches suggests that the mechanisms considered by Seager et al. (2003) do not require zonal symmetry for the zonal wind responses to SST anomalies and eddy–mean flow interactions. Instead, the atmospheric changes due to SST forcing and to eddy feedbacks could take place in distinct longitudinal domains along a given latitude circle.

The influences of the SST changes in IWP on the extratropical circulation have been highlighted in both L05 and the present study. The warm conditions in the tropical IWP during the 1997–2003 period could be a manifestation of the general upward temperature trend observed in that region in the past several decades (Knutson et al. 1999). The probable causes for this long-term signal include natural low-frequency variations of the atmosphere–ocean system, as well as climate changes induced by human activities. Experimentation with fully coupled models would be needed to identify the mechanisms contributing to the secular SST changes in the IWP. The output from such model runs, in which two-way air–sea interactions are to be incorporated in a comprehensive fashion, would also serve as a useful check of the validity of the findings reported in the present study, which does not include feedbacks of the atmospheric responses to the prescribed SST anomalies.

The diagnoses in this study suggest that, should the warming trend in IWP continue, the extratropical atmospheric anomalies during La Niña events would be progressively strengthened in the future, in view of the reinforcement between the responses to this particular configuration of SST forcing in the IWP and DTEP sectors. Conversely, the midlatitude response in El Niño episodes would gradually become weaker in the forthcoming decades, due to destructive interference between the signals originating from the IWP and DTEP regions. Further study is needed to delineate the impacts of sustained SST rise in IWP on the long-term trends in the amplitude of El Niño and La Niña responses.

It is noteworthy that the IWP region considered in this study consists of both the tropical portion of the Indo-western Pacific basin, as well as the two belts centered at 30°N and 30°S that extend eastward from the Asian and Australian coasts to 150°W (see Fig. 1b). With the inclusion of the latter pair of midlatitude zones, the meridional width of the IWP region is considerably broader than that of the DTEP region. Hence the zonal wind changes accompanying SST variations in IWP occur at higher latitudes than corresponding responses to SST forcing in DTEP. For instance, the pair of positive anomalies of $[u]$ are located at about 20° latitude during the 1997–98 El Niño in the DTEP experiment (Fig. 14d); whereas the corresponding features are found at 50° latitude in the IWP experiment (Fig. 14g). Such differences in the latitude of the zonal wind changes in the two experiments in turn determine the locations of eddy feedbacks and the eddy-induced tendencies (see section 6).

To assess the relative contributions of the SST anomalies in the tropical and midlatitude portions of the IWP region in modulating the atmospheric circulation, we have conducted an additional 10-member ensemble experiment in which the domain of variable SST forcing in the 1997–2004 period is confined to maritime grid points between 30°S and 30°N, and from the eastern African coast to 160°E. Thus, no SST variability is prescribed in this experiment in the extratropical por-

tions of the IWP region as originally defined in Fig. 1b (specifically, the zonal belts between 30° and 40° latitudes, as well as the pair of midlatitude extensions in the North and South Pacific between 160°E and 150°W). Except for a slight reduction in the 200-mb height response over the extratropical North Pacific, the results from these auxiliary model runs (not shown) are qualitatively similar to those presented for the full IWP experiment (Figs. 2d, 4d, 4h, and 7d). We hence conclude that tropical and subtropical portions of the IWP forcing play a more fundamental role in generating the atmospheric signals presented in this study. The stronger effects of the tropical SST anomalies in the IWP domain could in part be attributed to their influences on the strength of the jet stream over South Asia, which acts as a waveguide for zonally oriented and circumglobal wave trains (Branstator 2002).

Our investigation has been focused on the impacts of SST anomalies in the Pacific and Indian Ocean basins on the atmospheric circulation. It should be borne in mind that prevalent modes of atmosphere–ocean variability have also been identified in the Atlantic sector (Zebiak 1993; Chang et al. 1997), and that SST changes in that region are linked to prominent shifts in precipitation patterns in Africa and South America (Folland et al. 1986), as well as to the overlying atmospheric circulation (Chang et al. 2000). Due attention should therefore be devoted to assessing the role of Atlantic variability in the global-scale atmospheric changes documented in the present work. The nature of the interactions between the climate signals over the Atlantic, Pacific, and Indian Oceans also requires further study.

Acknowledgments. We thank Drs. I. Held, X. Jiang, J. Lu, R. Seager, P. Zurita-Gotor, and the official reviewers for perceptive comments on earlier versions of this manuscript.

REFERENCES

Alexander, M. A., I. Bladé, M. Newman, J. R. Lanzante, N.-C. Lau, and J. D. Scott, 2002: The atmospheric bridge: The influence of ENSO teleconnections on air–sea interaction over the global oceans. *J. Climate,* **15,** 2205–2231.

——, N.-C. Lau, and J. D. Scott, 2004: Broadening the atmospheric bridge paradigm: ENSO teleconnections to the tropical West Pacific–Indian Oceans over the seasonal cycle and to the North Pacific in summer. *Earth's Climate: The Ocean–Atmosphere Interactions, Geophys. Monogr.,* Vol. 147, Amer. Geophys. Union, 85–103.

Barlow, M., H. Cullen, and B. Lyon, 2002: Drought in central and southwest Asia: La Niña, the warm pool, and Indian Ocean precipitation. *J. Climate,* **15,** 697–700.

Blackmon, M. L., J. M. Wallace, N.-C. Lau, and S. L. Mullen, 1977: An observational study of the Northern Hemisphere wintertime circulation. *J. Atmos. Sci.,* **34,** 1040–1053.

Branstator, G., 2002: Circumglobal teleconnections, the jet stream waveguide, and the North Atlantic Oscillation. *J. Climate,* **15,** 1893–1910.

Chang, E. K. M., 1996: Mean meridional circulation driven by eddy forcings of different timescales. *J. Atmos. Sci.,* **53,** 113–125.

Chang, P., L. Ji, and H. Li, 1997: A decadal climate variation in the tropical Atlantic Ocean from thermodynamic air-sea interaction. *Nature,* **385,** 516–518.

——, R. Saravanan, L. Ji, and G. C. Hegerl, 2000: The effect of local sea surface temperatures on atmospheric circulation over the tropical Atlantic sector. *J. Climate,* **13,** 2195–2216.

Dai, A., I. Fung, and A. D. Del Genio, 1997: Surface observed global land precipitation variation during 1900–88. *J. Climate,* **10,** 2943–2962.

Folland, C., T. Palmer, and D. Parker, 1986: Sahel rainfall and world-wide sea temperatures: 1901-85. *Nature,* **320,** 602–606.

Frederiksen, J. S., 1983: Disturbances and eddy fluxes in Northern Hemisphere flows: Instability of three-dimensional January and July flows. *J. Atmos. Sci.,* **40,** 836–855.

GFDL Global Atmospheric Model Development Team, 2004: The new GFDL global atmosphere and land model AM2–LM2: Evaluation with prescribed SST simulation. *J. Climate,* **17,** 4641–4673.

Held, I. M., 1975: Momentum transport by quasi-geostrophic eddies. *J. Atmos. Sci.,* **32,** 1494–1497.

Hoerling, M. P., and A. Kumar, 2003: The perfect ocean for drought. *Science,* **299,** 691–694.

——, J. W. Hurrell, and T. Xu, 2001: Tropical origins for recent North Atlantic climate change. *Science,* **292,** 90–92.

——, ——, T. Xu, G. T. Bates, and A. S. Phillips, 2004: Twentieth century North Atlantic climate change. Part II: Understanding the effect of Indian Ocean warming. *Climate Dyn.,* **23,** 391–405.

Horel, J. D., and J. M. Wallace, 1981: Planetary-scale atmospheric phenomena associated with the Southern Oscillation. *Mon. Wea. Rev.,* **109,** 813–829.

Huffman, G. J., R. F. Adler, A. Chang, R. Ferraro, A. Gruber, A. McNab, B. Rudolf, and U. Schneider, 1997: The Global Precipitation Climatology Project (GPCP) combined precipitation dataset. *Bull. Amer. Meteor. Soc.,* **78,** 5–20.

Kalnay, E., and Coauthors, 1996: The NCEP/NCAR 40-Year Reanalysis Project. *Bull. Amer. Meteor. Soc.,* **77,** 437–471.

Kawamura, R., T. Matsuura, and I. Satoshi, 2001a: Role of equatorially asymmetric sea surface temperature anomalies in the Indian Ocean in the Asian summer monsoon and El Niño-Southern Oscillation coupling. *J. Geophys. Res.,* **106,** 4681–4693.

——, ——, and ——, 2001b: Interannual atmosphere-ocean variations in the tropical western North Pacific relevant to the Asian summer monsoon-ENSO coupling. *J. Meteor. Soc. Japan,* **79,** 883–898.

Klein, S. A., B. J. Soden, and N.-C. Lau, 1999: Remote sea surface temperature variations during ENSO: Evidence for a tropical atmospheric bridge. *J. Climate,* **12,** 917–932.

Kumar, A., and M. P. Hoerling, 2003: The nature and causes for the delayed atmospheric response to El Niño. *J. Climate,* **16,** 1391–1403.

——, S. Schubert, and M. J. Suarez, 2003: Variability and predictability of 200-mb seasonal mean heights during summer and winter. *J. Geophys. Res.,* **108,** 4169, doi:10.1029/2002JD002728.

Knutson, T. R., T. L. Delworth, K. W. Dixon, and R. J. Stouffer, 1999: Model assessment of region surface temperature trends (1947–1997). *J. Geophys. Res.,* **104,** 30 981–30 996.

Lau, N.-C., 1988: Variability of the observed midlatitude storm tracks in relation to the low-frequency changes in the circulation pattern. *J. Atmos. Sci.,* **45,** 2718–2743.

——, and M. J. Nath, 1994: A modeling study of the relative roles of tropical and extratropical SST anomalies in the variability of the global atmosphere–ocean system. *J. Climate,* **7,** 1184–1207.

——, and ——, 2000: Impact of ENSO on the variability of the Asian–Australian monsoons as simulated in GCM experiments. *J. Climate,* **13,** 4287–4309.

——, and ——, 2003: Atmosphere–ocean variations in the Indo-Pacific sector during ENSO episodes. *J. Climate,* **16,** 3–20.

——, A. Leetmaa, M. J. Nath, and H.-L. Wang, 2005: Influences of ENSO-induced Indo-Western Pacific SST anomalies on extratropical atmospheric variability during the boreal summer. *J. Climate,* **18,** 2922–2942.

Lu, J., R. J. Greatbatch, and K. A. Peterson, 2004: Trend in Northern Hemisphere winter atmospheric circulation during the last half of the twentieth century. *J. Climate,* **17,** 3745–3760.

Nigam, S., 2003: Teleconnections. *Encyclopedia of Atmospheric Sciences,* J. R. Holton, J. A. Curry, and J. A. Pyle, Eds., Vol. 6, Academic Press, 2243–2269.

Rodwell, M., D. Rowell, and C. Folland, 1999: Oceanic forcing of the wintertime North Atlantic Oscillation and European climate. *Nature,* **398,** 320–323.

Ropelewski, C. F., and M. S. Halpert, 1989: Precipitation patterns associated with the high index phase of the Southern Oscillation. *J. Climate,* **2,** 268–284.

Saji, N. H., B. N. Goswami, P. N. Vinayachandran, and T. Yamagata, 1999: A dipole mode in the tropical Indian Ocean. *Nature,* **401,** 360–363.

Schubert, S. D., M. J. Suarez, P. J. Peigon, M. A. Kistler, and A. Kumar, 2002: Predictability of zonal means during boreal summer. *J. Climate,* **15,** 420–434.

——, M. J. Suarez, P. J. Pegion, R. D. Koster, and J. T. Bacmeister, 2004: Causes of long-term drought in the U.S. Great Plains. *J. Climate,* **17,** 485–503.

Seager, R., N. Harnik, Y. Kushnir, W. Robinson, and J. Miller, 2003: Mechanisms of hemispherically symmetric climate variability. *J. Climate,* **16,** 2960–2978.

Simmons, A. J., 1982: The forcing of stationary wave motion by tropical diabatic heating. *Quart. J. Roy. Meteor. Soc.,* **108,** 503–534.

Sutton, R. T., and D. L. R. Hodson, 2003: Influences of the ocean on North Atlantic climate variability 1871–1999. *J. Climate,* **16,** 3296–3313.

——, and ——, 2005: Atlantic Ocean forcing of North American and European summer climate. *Science,* **309,** 115–118.

Ting, M., and L. Yu, 1998: Steady response to tropical heating in wavy linear and nonlinear baroclinic models. *J. Atmos. Sci.,* **55,** 3565–3582.

Trenberth, K. E., 1986: An assessment of the impact of transient eddies on the zonal flow during a blocking episode using localized Eliassen–Palm flux diagnostics. *J. Atmos. Sci.,* **43,** 2070–2087.

——, and G. W. Branstator, 1992: Issues in establishing causes of the 1988 drought over North America. *J. Climate,* **5,** 159–172.

——, G. W. Branstator, D. Karoly, A. Kumar, N.-C. Lau, and C. Ropelewski, 1998: Progress during TOGA in understanding and modeling global teleconnections associated with tropical sea surface temperatures. *J. Geophys. Res.,* **103,** 14 291–14 324.

Vallis, G. K., E. P. Gerber, P. J. Kushner, and B. A. Cash, 2004: A mechanism and simple dynamical model of the North Atlantic Oscillation and annular modes. *J. Atmos. Sci.,* **61,** 264–280.

Weare, B. C., 1979: A statistical study of the relationships between ocean surface temperatures and the Indian monsoon. *J. Atmos. Sci.,* **36,** 2279–2291.

Webster, P. J., A. M. Moore, J. P. Loschnigg, and R. R. Leben, 1999: Coupled ocean-atmosphere dynamics in the Indian Ocean during 1997–98. *Nature,* **401,** 356–360.

Zebiak, S. E., 1993: Air–sea interaction in the equatorial Atlantic region. *J. Climate,* **6,** 1567–1586.